UNIVERSITY OF CALIFORNIA
RIVERSIDE

Efficient Spin-Pumping in Ultrafast Magnetic Systems

A Dissertation submitted in partial satisfaction
of the requirements for the degree of

Doctor of Philosophy

in

Physics

by

Mingda Guo

June 2024

Dissertation Committee:

Dr. Ran Cheng, Chairperson
Dr. Yongtao Cui
Dr. Igor Barsukov

The Dissertation of Mingda Guo is approved:

Committee Chairperson

University of California, Riverside

Acknowledgments

Completing a Ph.D. is indeed a long and arduous journey filled with the joy of breakthroughs and the confusion of stumbling blocks. Along this path, I have been fortunate to receive selfless support from many individuals, for which I am deeply grateful.

First and foremost, I would like to express my heartfelt gratitude to my advisor, Professor Ran Cheng. Transitioning from a student, who primarily learned from textbooks, to a researcher, who explores the unknown, was incredibly challenging. Being far from home in a foreign land, Professor Cheng's immense patience and support helped me navigate through this thorny path. When I embarked on advanced theoretical explorations during my Ph.D., Professor Cheng devoted his entire energy to mentor me closely, helping me master various skills step by step.

The year 2020 brought a CoVid-19 pandemic that changed much of our lives, compelling us to face a comprehensive transformation. After a difficult decision, I chose to return to my country to be with my family. Despite the distance of 20,000 kilometers and a time difference of 16 hours, Professor Cheng continued to support me tirelessly, often working until midnight. His guidance covered all aspects of my life, from academic to personal. I consider myself incredibly lucky to have met Professor Cheng during the most crucial phase of my academic career.

Additionally, I would like to thank all the members of our research group for their assistance, especially Dr. Yuhang Li. Joining the group in the same year as a postdoctoral fellow, Dr. Li provided me with comprehensive support in my research with his expertise.

On a personal note, I am immensely grateful to my family for their deep love and

support. My grandmother, who passed away in 2020 without my being able to see her one last time, remains one of my greatest regrets.

I am also blessed to have met my life partner, Jingyi Sun, during my academic journey. Her tenderness and encouragement helped me through the final year of my studies. Love in a foreign land is a challenge but also a testament to our relationship. Regardless of success or failure, Jingyi has always stood by me, encouraging me to be brave. I believe this is a promise that will accompany us for a lifetime.

To all who have supported me—my mentor, colleagues, friends, and family—I owe a deep debt of gratitude. This dissertation would not have been possible without your unwavering support and belief in my abilities. Thank you from the bottom of my heart.

This is a gift for my grandma, who loved me her entire life. I wish her peace and rest in heaven.

ABSTRACT OF THE DISSERTATION

Efficient Spin-Pumping in Ultrafast Magnetic Systems

by

Mingda Guo

Doctor of Philosophy, Graduate Program in Physics
University of California, Riverside, June 2024
Dr. Ran Cheng, Chairperson

Spintronics explores the interaction between magnetization dynamics and electron transport, primarily in ferromagnetic (FM) materials. This dissertation extends spintronics to antiferromagnetic (AF) materials, which are underexplored and lack comprehensive theoretical support. We investigate dc spin pumping in the canted easy-plane antiferromagnet α-Fe_2O_3, facilitated by the Dzyaloshinskii–Moriya interaction.

Additionally, we examine NiO under a magnetic field below the spin-flop transition, demonstrating that field alteration of resonance polarization enables robust sub-terahertz spin pumping akin to easy-axis AFs. Besides, an applied magnetic field significantly lowers the threshold for Néel vector auto-oscillation via spin-transfer torques, enhancing potential for device innovation in the sub-terahertz spectrum.

This comprehensive analysis not only deepens our understanding of AF spintronics but also paves the way for the development of innovative spintronic devices leveraging the unique properties of antiferromagnetic materials. Finally, the dissertation extends its examination to the physical properties of two-sublattice ferrimagnets (FIMs) and antifer-

romagnetic van der Waals materials within the context of two-dimensional (2D) layered systems. This exploration further broadens the study of spintronics beyond traditional AF materials.

Contents

List of Figures

Chapter 1

Introduction

1.1 Overview of Antiferromagnetic Spintronics

Spintronics, blending the principles of electron spin with electronics, marks a pivotal advancement in modern technology. Its influence is profoundly felt in areas like data storage, memory devices, quantum computing, nano-technology, etc[71, 9, 50, 7, 19]. This innovative field harnesses not only the charge of electrons, as in traditional electronics, but also their spin - a quantum property that offers new dimensions for device functionality. The true potential of spintronics is its capacity to outperform conventional electronic devices in terms of speed, efficiency, and scalability, heralding a new era in technological development. Additionally, spintronics introduces reduced power consumption and heat generation, addressing two of the most pressing challenges in modern electronic design. This reduced power requirement opens up possibilities for more sustainable and energy-efficient technologies, a crucial consideration in the context of global energy concerns. This backdrop of innovation and exploration in spintronics sets the stage for a recent and significant shift in

the field's focus. In recent years, research has increasingly centered on enhancing the control and functionality of magnetic materials, with a particular emphasis on ferromagnetic substances[15, 22, 43]. These materials, known for their notable macroscopic magnetization, have been central to conventional spintronics applications. However, paralleling these advancements, the less-explored antiferromagnetic materials, characterized by their zero net magnetization and staggered magnetic fields, have begun to capture the attention of researchers. This shift represents a paradigm change in the field, acknowledging the untapped potential and novel functionalities that antiferromagnetic materials bring to the forefront of spintronics research[41, 1, 28, 27, 74]. Building on the paradigm shift towards antiferromagnetic materials in spintronics research, the appeal of these materials lies in their diverse and significant advantages. Antiferromagnetic materials are particularly notable for their enhanced dynamics and stability, qualities that make them ideal for applications requiring high speed and high density. A key attribute of these materials is their inherent absence of stray magnetic fields, a crucial advantage for reducing magnetic interference in densely packed electronic circuits. This characteristic becomes increasingly important as the trend moves towards more miniaturized and integrated technological systems.

The exploration of these uncharted territories in antiferromagnetic spintronics is not merely academic curiosity but is driven by the potential revolutionary impact on technology[68]. Addressing the identified gaps will not only deepen our fundamental understanding of spin physics in antiferromagnets but also pave the way for groundbreaking applications in data storage, quantum computing, and nano-technology. By unlocking the secrets of antiferromagnetic materials, particularly in spin pumping and spin dynamics, we

can develop faster, more efficient, and more stable spintronic devices. This research could lead to significant advancements in the field, offering new paradigms in the design and functionality of electronic devices. The pursuit of these questions is, therefore, both a scientific imperative and a step towards technological innovation.

1.2 Spin Pumping

Building upon the foundational concepts introduced in antiferromagnetic spintronics, spin pumping emerges as a key phenomenon in this domain. It involves the transfer of angular momenta from a magnetic material, whether ferromagnetic or antiferromagnetic, to a non-magnetic layer, typically a heavy metal. This transfer process is primarily initiated by the magnetization precession within the magnetic layer, which in turn triggers the generation of a spin current into the adjacent non-magnetic layer[14, 1, 26, 38, 63]. At these interfaces, spin-orbit coupling plays a significant role. This coupling, resulting from the interaction between an electron's spin and its orbital momentum within the material's potential, is notably more pronounced at interfaces. This is particularly true in areas where there is a significant shift in the potential landscape. Understanding the intricacies of spin pumping mechanisms is crucial, as it enables effective manipulation and control of spin currents. Such control is indispensable for the development and advancement of sophisticated technological applications, marking spin pumping as a key process in the advancement of spintronic technologies.

In the specific context of antiferromagnetic materials, the dynamics of spin pumping present distinct characteristics, setting them apart from their ferromagnetic counterparts[43,

26, 73, 67]. Antiferromagnets (AFs) operate at significantly higher frequencies, in the terahertz (THz) range, paving the way for ultrafast information processing and communication capabilities. Additionally, the absence of stray fields in AFs enhances their robustness against magnetic disturbances, making them highly appealing for next-generation data storage technologies. However, a notable challenge in antiferromagnets is the fact that their net magnetization, m, typically vanishes in equilibrium in homogeneous structures and remains negligible even when the system is slightly perturbed around this equilibrium. Consequently, the dynamics of spin pumping in these materials cannot be effectively described using net magnetization. Instead, the Néel vector n, which represents the difference in the magnetic moments of the antiparallel sublattices, is employed to characterize spin-pumping dynamics in antiferromagnetic materials.

To further probe these unique dynamics, additionally, a range of experimental methods has been employed, offering deeper insights into the behavior of spin pumping in antiferromagnetic materials. These methods include ferromagnetic resonance (FMR) techniques[73, 30], which are instrumental in exciting and measuring spin waves, time-resolved magneto-optical Kerr effect (MOKE) microscopy for observing magnetic domain dynamics[40, 2], and spin-torque ferromagnetic resonance (ST-FMR)[75], which sheds light on the impact of spin torque on magnetic dynamics. Recent studies employing these techniques have been pivotal in unraveling the complexities of spin dynamics in antiferromagnetic materials and their broader implications for spintronic devices. Each experimental approach provides distinct insights into the behavior of spins, contributing vitally to a more comprehensive understanding of spin pumping and its myriad potential applications.

1.3 Spin-transfer Torque

Following the introduction of spin pumping and its implications in antiferromagnetic materials, its Onsager reciprocal mechanism, spin-transfer torque (STT), comes into focus[39, 47, 48]. STT represents a back-action of an incident spin current from the normal metal that exerts on the interfacial magnetic moments, thereby allowing for the control of magnetic states without the need for external magnetic fields[74, 1, 43, 53]. This mechanism stands at the forefront of revolutionizing memory and logic devices, making it a cornerstone in the development of energy-efficient and high-speed spintronic technologies.

Integral to understanding STT are two primary components: field-like torque and damping-like torque. The field-like torque acts perpendicularly to the magnetic moments and can be thought of as an effective magnetic field that influences the direction of these moments. This torque can induce precessional motion of the magnetization, playing a significant role in dynamic switching processes. On the other hand, the damping-like torque aligns parallel or antiparallel to the magnetization, providing a mechanism for energy dissipation. It directly influences the damping of the magnetic moment's precession, thereby impacting the stability and speed of the magnetic switching.

In the specific context of antiferromagnetic materials, STT exhibits notably complex and nuanced characters. While STT in ferromagnets (Fs) involves the alignment of spins in a uniform direction, AFs present a more complex scenario due to their alternating spin alignment. This difference fundamentally alters the dynamics of how spin-polarized currents interact with the material's magnetic moments. In AFs, STT can induce changes in the Néel vector n as opposed to merely reorienting uniform magnetization as in Fs.

This distinction leads to subtler and more intricate manipulations of the magnetic state, requiring precise control over the spin current. Furthermore, antiferromagnetic materials typically respond to STT at an exceptionally rapid pace, operating within the terahertz frequency range. This rapid response time positions antiferromagnets as ideal candidates for applications requiring ultrafast switching, a significant advantage over their ferromagnetic counterparts.

Owing to their inherent properties, the integration of Spin Transfer Torque (STT) in antiferromagnetic auto-oscillators offers a plethora of significant advantages[13, 61, 57]. Foremost among these is the ability of these auto-oscillators to operate at terahertz frequencies. This characteristic enables them to achieve oscillation frequencies considerably higher than those attainable in ferromagnetic systems. Such high-frequency operation is indispensable for the creation of ultrafast signal processing components and the advancement of sophisticated communication technologies. Moreover, the intrinsic nature of antiferromagnetic materials, characterized by their absence of net magnetization, endows them with enhanced robustness against external magnetic field disturbances. This inherent stability is of paramount importance in applications that demand consistent and reliable oscillation frequencies.

1.4 Spin-charge Conversion

Building upon the insights gained from the exploration of Spin Transfer Torque, we venture into the realm of spin-charge conversion. This process stands at the forefront of spintronic device functionality, acting as a vital bridge that connects spin-based phenomena

with charge-based electronics. Among the various mechanisms at play, some have garnered significant attention for their pivotal roles. A prime example is the Inverse Spin Hall Effect (ISHE), which is essential for converting spin currents into charge currents within magnetic materials. This effect emerges from the spin-orbit interaction, where the scattering of spin-polarized electrons leads to the generation of a transverse electric voltage[59, 52, 29]. Additionally, the Rashba-Edelstein Effect (REE) becomes significant in systems exhibiting strong spin-orbit coupling and structural inversion asymmetry. The application of an electric field in such materials induces spin polarization, thereby converting charge current into spin accumulation[65, 16, 76]. The REE is particularly noted for its ability to control spin currents electrically, offering a complementary approach to the magnetic manipulation techniques. This dual control mechanism enhances the versatility and efficacy of spintronic devices, marrying the realms of electric and magnetic spin manipulations.

In antiferromagnetic materials, the unique attributes of both the ISHE and the REE distinctly differentiate them from their behavior in ferromagnetic materials. Primarily, the zero net magnetization characteristic of AFs implies that spin currents generated or influenced by the ISHE are not as overtly discernible as in Fs. This subtlety, however, is complemented by an advantage: AFs exhibit a reduced susceptibility to external magnetic interference. This property potentially allows for more accurate and stable detection and conversion of spin currents, making antiferromagnetic materials highly promising for applications in high-precision spintronics.

Additionally, while the Spin Hall Effect is known to generate spin-polarized currents, leading to effective spin–orbit torques in ferromagnetic layers, the REE in antiferro-

magnets offers a different mechanism of action. The REE has been proposed as a method to induce non-equilibrium spin polarization through an electrical current in solids lacking inversion symmetry. In the context of noncentrosymmetric antiferromagnetic materials, this effect can lead to current-induced staggered spin polarization and spin–orbit torque. Such dynamics can cause the magnetic moments in antiferromagnetic materials to reorient perpendicularly, presenting a novel approach to manipulating their magnetic states. This exploration into current-induced effects in antiferromagnets underscores their potential for innovative applications in spintronics, particularly in areas where precise control of magnetic moments is essential.

1.5 Van der Waals Antiferromagnets

Following our in-depth exploration of spin-charge conversion mechanisms in antiferromagnetic materials, the focus now shifts to a cutting-edge topic in the field of spintronics: van der Waals(vdW) AFs. vdW AFs are characterized by their layered structures, held together by weak van der Waals forces. This aspect gives rise to distinctive physical properties that set them apart from conventional antiferromagnetic materials[62, 37, 49, 23, 8].

In stark contrast to traditional magnetic thin films, two-dimensional (2D) materials exhibit a remarkable degree of decoupling from their substrates. This independence allows for enhanced electrical control, mechanical flexibility, and opportunities for chemical functionalization. These attributes render 2D magnets not only accessible and engineerable but also highly integrable into novel heterostructures. Such integration can lead to previously unattainable properties and applications. For instance, the development of atomically

thin magneto-optical and magnetoelectric devices opens new avenues in ultracompact spintronics, on-chip optical communications, and quantum computing - realms where the unique characteristics of 2D materials can be fully leveraged.

Van der Waals Antiferromagnets (AFs), a significant class of these 2D materials, demonstrate distinctly different magnetic interactions compared to conventional antiferromagnets. In Van der Waals AFs, the magnetic interactions are more localized, a stark deviation from the strong and long-range interactions typical in traditional antiferromagnets. This localization of interactions bestows upon these materials unique magnetic behaviors, such as heightened sensitivity to external stimuli. Such sensitivity facilitates nuanced and precise control over their magnetic states, crucial for applications that demand meticulous magnetic manipulation.

Additionally, the weaker interlayer van der Waals interactions in these materials result in reduced exchange coupling between the staggered sublattices. This aspect significantly influences the dynamics of Van der Waals AFs, bringing them into the low sub-terahertz (sub-THz) frequency regime. This lower frequency range not only makes the antiferromagnetic fundamental dynamics more accessible for experimental study but also opens up possibilities for practical applications that were previously hindered by the higher operational frequencies of traditional antiferromagnets.

1.6 Motivation and Outline

As we delve deeper into the burgeoning field of antiferromagnetic spintronics, it becomes evident that while significant strides have been made in both understanding funda-

mental spin dynamics and mechanisms and practical technical breakthroughs, substantial gaps remain in our knowledge. Fully harnessing the potential of antiferromagnetic materials in the domain of spintronics is replete with unique challenges. Firstly, the ultrafast properties of antiferromagnets place exceptionally high and sophisticated demands on both experimental tools and technological devices, often requiring capabilities to handle such high-frequency dynamics. Additionally, the vanishing magnetization in antiferromagnetic materials, which could be considered an advantage, ironically poses a significant challenge. It complicates the detection of antiferromagnetic order and, consequently, the development of effective reading mechanisms in device engineering. Furthermore, integrating these materials into existing technological infrastructures is a complex task. These materials need to possess appropriate antiferromagnetic ordering temperatures, compatibility with existing technologies, and electronic properties that are conducive to practical applications. These challenges highlight the ongoing need for innovation and exploration in the realm of antiferromagnetic spintronics.

In this dissertation, a comprehensive approach to antiferromagnetic spintronics is elucidated. The core objective is to paint a detailed picture of the ultrafast properties of antiferromagnets and their related materials. Chapter Two delves into the enhancement of spin pumping, taking the Dzyaloshinskii-Moriya (DM) interaction in α-Fe_2O_3 as a case study. Chapter Three shifts the focus to the feasibility of achieving spin pumping in easy-plane antiferromagnets, exemplified by NiO. In chapters Four and Five, alternative materials - ferrimagnets and 2D magnets are highlighted. These materials offer significant advantages over traditional antiferromagnetic counterparts, potentially paving the way for ultrafast

operational capabilities. Finally, Chapter Six synthesizes the discussions from the preceding chapters, concluding with an in-depth analysis of ultrafast operations in antiferromagnetic spintronics. This dissertation aims to contribute a significant body of knowledge to the field, addressing both theoretical and practical aspects of antiferromagnetic spintronics and its future trajectory.

Chapter 2

Spin Pumping Enhanced by Dzyaloshinskii-Moriya Interaction

As we delve further into the intricacies of spin pumping within the realm of antiferromagnetic spintronics, the unique case of easy-plane antiferromagnets comes to the forefront. These materials, while possessing certain advantageous properties for spin pumping, also present their own set of challenges, underscoring the complexities involved in fully harnessing their potential.

Easy-plane antiferromagnets are characterized by their relatively small magnon gaps and accessible resonant frequencies, which at first glance, make them seemingly ideal candidates for efficient spin pumping. Additionally, easy-plane antiferromagnets are abundant in nature and can be prepared and preserved with relative ease, adding to their appeal as materials of choice in spintronic research.

However, this advantage is counterbalanced by a significant limitation. The inher-

ent spin dynamics within easy-plane antiferromagnets are predominantly linearly polarized. This polarization is a key point of divergence from the more commonly studied uniaxial antiferromagnets, where the spins are circular polarized [38]. The linear polarization in easy-plane antiferromagnets has long been perceived as a hindrance to effective spin pumping, as it contrasts with the conventional mechanisms observed in uniaxial systems.

This perception presents a notable challenge in the field: how to effectively leverage the advantageous aspects of easy-plane antiferromagnets for spin pumping while overcoming the inherent difficulties posed by their unique spin dynamics. The exploration of this challenge not only deepens our understanding of antiferromagnetic spintronics but also opens up potential pathways for innovative solutions and advanced applications in spintronic devices.

2.1 Easy-plane Antiferromagnet with Dzyaloshinskii-Moriya Interaction

The Dzyaloshinskii-Moriya (DM) interaction, originating from spin-orbit coupling in systems with broken inversion symmetry, is an anti-symmetric exchange interaction first proposed by Igor Dzyaloshinskii and further developed by Toru Moriya. In antiferromagnetic systems, the DM interaction plays a crucial role in stabilizing complex spin textures and promoting non-collinear spin arrangements, significantly influencing the magnetic properties and dynamics of these materials. This interaction is key to understanding various phenomena in antiferromagnets, from spin canting to the emergence of exotic magnetic states.

Consider an external magnetic field H applied along the y-axis in the magnetic

easy plane of an AF. The effective free energy to be re-expressed as:

$$\begin{aligned}\epsilon = \omega_J \mathbf{m}_1 \cdot \mathbf{m}_2 + \frac{\omega_K}{2}\left[(\hat{\mathbf{z}}\cdot\mathbf{m}_1)^2 + (\hat{\mathbf{z}}\cdot\mathbf{m}_2)^2\right] - \frac{\omega_A}{2}\left[(\hat{\mathbf{x}}\cdot\mathbf{m}_1)^2 + (\hat{\mathbf{x}}\cdot\mathbf{m}_2)^2\right] \\ - \omega_D \hat{\mathbf{z}}\cdot(\mathbf{m}_1 \times \mathbf{m}_2) - \omega_H \hat{\mathbf{y}}\cdot(\mathbf{m}_1 + \mathbf{m}_2)\end{aligned} \tag{2.1}$$

where, $\omega_J = \gamma H_J$ represents the exchange frequency, with $\gamma/2\pi$ being the gyromagnetic ratio and H_E denoting the exchange field. Similarly, $\omega_K = \gamma H_K$ and $\omega_A = \gamma H_A$ correspond to the frequencies of the hard-axis and easy-axis anisotropies, respectively. Additionally, $\omega_D = \gamma H_D$ represents the DM field, and $\omega_H = \gamma H$ is the Larmor frequency due to the applied magnetic field. Here, the coordinate system is depicted in Fig. 2.1.

In the exchange limit, where the exchange interaction significantly exceeds any other interactions, the free energy can be minimized to obtain a canted ground state. In this state, the magnetic moments are given by $\bar{m}_1 = \{\cos\phi, \sin\phi, 0\}$ and $\bar{m}_2 = \{-\cos\phi, \sin\phi, 0\}$, where the canting angle ϕ is approximately $\frac{(\omega_D+\omega_H)}{2\omega_E}$. To further analyze the dynamics and, subsequently, the spin-pumping mechanisms, we consider the precessional motions of the vectors $\mathbf{m}_1$ and $\mathbf{m}_2$ around their equilibrium directions. The behavior of the system is effectively described by the following two coupled Landau-Lifshitz-Gilbert (LLG) equations:

$$\dot{\mathbf{m}}_1 = \mathbf{m}_1 \times [\omega_E \mathbf{m}_2 + (\omega_K - \omega_D \mathbf{m}_2\cdot)\hat{\mathbf{z}} - \omega_A \hat{\mathbf{x}} - \omega_H \hat{\mathbf{y}}] + \alpha \mathbf{m}_1 \times \dot{\mathbf{m}}_1 + \gamma h_{\mathrm{rf}} \times \mathbf{m}_1, \tag{2.2a}$$

$$\dot{\mathbf{m}}_2 = \mathbf{m}_2 \times [\omega_E \mathbf{m}_1 + (\omega_K + \omega_D \mathbf{m}_1\cdot)\hat{\mathbf{z}} - \omega_A \hat{\mathbf{x}} - \omega_H \hat{\mathbf{y}}] + \alpha \mathbf{m}_2 \times \dot{\mathbf{m}}_2 + \gamma h_{\mathrm{rf}} \times \mathbf{m}_2. \tag{2.2b}$$

Here, the microwave magnetic field is denoted as $h_{\mathrm{rf}} = h_{\mathrm{rf}} e^{i\omega t}\hat{\mathbf{x}}$ and is polarized along the x-axis. To simplify the analysis, we linearize the LLG equations by approximating $\mathbf{m}_1 \approx \bar{\mathbf{m}}_1 + \delta\mathbf{m}_1 e^{i\omega t}$ and $\mathbf{m}_2 \approx \bar{\mathbf{m}}_2 + \delta\mathbf{m}_2 e^{i\omega t}$, where $\delta\mathbf{m}_i$ is orthogonal to $\bar{\mathbf{m}}_i$ (for $i = 1, 2$) and ω represents the angular frequency of the microwave. The linearization truncates the

equations at the first order in $\delta\mathbf{m}_i$. Consequently, the LLG equations transform into an eigenvalue problem, allowing us to derive the precession modes of the magnetization vectors based on the eigenmodes of LLG equations.

In the absence of DM interaction, the sublattice magnetic moments, m_1 and m_2, undergo right-handed elliptical precession around their equilibrium directions. The major and minor axes of these precessional ellipses are aligned along the y-axis and z-axis, respectively. Without a sufficiently strong external field to induce significant canting of m_1 and m_2 along the y-axis, the total magnetic moment $m = m_1 + m_2$ primarily exhibits linear oscillation along the z-direction. Consequently, this configuration leads to an AC spin pumping phenomenon where the DC component is negligible. Additionally, due to polarization mismatch, an x-polarized microwave magnetic field cannot effectively drive resonance with $m(t)$, a feature typical of conventional easy-plane antiferromagnets such as NiO and MnO.

However, when the DM field H_D is introduced, the magnetic moments m_1 and m_2 become canted towards the y-axis at equilibrium, leading to an elliptical precession around these canted directions. Consequently, this results in the magnetic moment $m(t)$ describing an elliptical orbit around the y-axis. Crucially, the elliptical trajectory of the canted magnetic moment gains a significant projection along the x-axis. This change permits a Néel vector (n) polarized microwave magnetic field to effectively resonate with the acoustic mode, facilitating DC spin pumping. As the DM field H_D intensifies, the precession of $m(t)$ evolves towards a more circular path, which in turn markedly enhances the efficiency of DC spin pumping, surpassing that of conventional easy-plane antiferromagnets.

2.2 Spin Injection

Driven by the resonant field, the canted magnetic moment $\mathbf{m} = \bar{\mathbf{m}} + \delta\mathbf{m}$ components undergo rotational motions about the y-axis. This dynamic leads to the following mathematical expressions:

$$\delta m_x = \mathrm{Re}[\tilde{m}_x] = \mathrm{Re}[|m_x|e^{i(\omega t+\phi_x)}] \equiv \mathrm{Re}[\chi_{xx}h_{\mathrm{rf}}], \tag{2.3a}$$

$$\delta m_z = \mathrm{Re}[\tilde{m}_z] = \mathrm{Re}[|m_z|e^{i(\omega t+\phi_z)}] \equiv \mathrm{Re}[\chi_{zx}h_{\mathrm{rf}}], \tag{2.3b}$$

where $\chi_{xx} = \frac{\tilde{m}_{1x}+\tilde{m}_{2x}}{h_{\mathrm{rf}}}$ and $\chi_{zx} = \frac{\tilde{m}_{1z}+\tilde{m}_{2z}}{h_{\mathrm{rf}}}$ represent components of the dynamical susceptibility tensor. The phase factors ϕ_x and ϕ_z are appropriately adjusted relative to the magnetic field h_{rf}. While the dynamical susceptibility tensor can be resolved analytically, the resulting expression is complex; therefore, we opt for numerical calculation. In our device geometry depicted in Fig. 2.2, the direct current (dc) spin pumping is proportional to:

$$\begin{aligned}
\hat{\mathbf{y}} \cdot (\mathbf{m} \times \dot{\mathbf{m}}) &= \delta m_z \dot{\delta m}_x - \delta m_x \dot{\delta m}_z \\
&= \omega |m_x||m_z| \left[\cos(\omega t + \phi_x)\sin(\omega t + \phi_z) - \sin(\omega t + \phi_x)\cos(\omega t + \phi_z)\right] \\
&= \omega |\chi_{xx}||\chi_{zx}| \sin(\phi_z - \phi_x) h_{\mathrm{rf}}^2 \\
&= \omega \mathrm{Im}[\chi_{xx}^* \chi_{zx}] h_{\mathrm{rf}}^2
\end{aligned} \tag{2.4}$$

In the standard framework, the direct current (dc) component of the pumped spin current density, I_s^y, is directly related to the normalized vector $\hat{\mathbf{m}} \approx \frac{\omega_E}{\omega_D+\omega_H}\mathbf{m}$. The relationship is expressed as follows:

$$I_s^y = \hbar g_r \hat{\mathbf{y}} \cdot (\hat{\mathbf{m}} \times \frac{d\hat{\mathbf{m}}}{dt}) = \hbar g_r \omega \mathrm{Im}[\chi_{xx}^* \chi_{zx}] \left(\frac{\omega_E}{\omega_D + \omega_H}\right)^2 h_{\mathrm{rf}}^2 \approx \hbar g_r f \mathrm{Im}[\chi_{xx}^* \chi_{zx}] \left(\frac{h_{\mathrm{rf}} H_E}{H_D}\right)^2 \tag{2.5}$$

Here, $f = \frac{\omega}{2\pi}$ denotes the driving frequency, and g_r represents the spin-mixing conductance. This equation provides a quantitative measure of the pumped spin current density in terms of the driving frequency, the material's intrinsic properties, and the applied microwave magnetic field. The expression highlights the critical role of the dynamical susceptibility components in the spin-pumping mechanism.

2.3 Spin Pumping Signal

The spin current injected into the system, denoted as I_s, is converted into a charge current through the inverse spin Hall effect. This conversion process is quantified by the voltage signal V_{SP}, which is given by the equation:

$$V_{\mathrm{SP}} = \xi_r \frac{L\Theta_{\mathrm{SH}}^{\mathrm{eff}}\lambda}{2\pi} \tanh\left(\frac{d_N}{2\lambda}\right) |h_{\mathrm{rf}}|^2 \tag{2.6}$$

Here, e represents the electron charge, while L, θ_{SH}, λ, ρ, and d_N signify the length of the heavy-metal layer, the effective spin Hall angle, the spin diffusion length, the resistivity, and the thickness of the heavy-metal layer, respectively. The term $\tilde{g}_r$, defined as

$$\tilde{g}_r = \frac{g_r}{\left[1 + \left(\frac{2\lambda e^2 \rho g_r}{\hbar}\right) \coth\left(\frac{d_N}{\lambda}\right)\right]}, \tag{2.7}$$

represents the effective spin-mixing conductance which accounts for the spin backflow effect in the heavy-metal layer. This backflow is an essential consideration in accurately determining the efficiency of the spin-to-charge current conversion.

In analysis, $\xi = 2\pi f \mathrm{Im}[\chi_{xx}\chi_{zx}]$ is introduced as the spin-pumping susceptibility, a measure for quantifying the efficiency with which microwave power is converted into a DC spin current density. The value of ξ is highly sensitive to the polarization dynamics

of $m(t)$, which in turn are influenced by the Dzyaloshinskii-Moriya (DM) field H_D, the driving frequency f, and the magnitude of the external magnetic field H. Remarkably, the presence of the DM interaction has a profound effect on the system's response; it not only substantially increases the peak value ξ_p but also concurrently reduces the resonance field H_{res}. This relationship is graphically depicted in the insets, where an increase in H_D from zero to its maximum value H_D^{Max} results in a sevenfold decrease in H_{res}, while ξ_p experiences a dramatic increase by a factor of nearly 350. Such an extraordinary enhancement is a clear testament to the crucial role played by the DM interaction in amplifying the observed DC spin-pumping signals.

2.4 Gilbert Damping Esitimation

To refine the approximation of the Gilbert damping coefficient for the material under study, a comparative analysis between experimental data and theoretical projections has been conducted. Theoretical full width at half maximum (FWHM) values are extracted by critically examining computational curves. Iterative adjustments to the Gilbert damping coefficient bring theoretical curves into agreement with experimental findings, as depicted in Fig. 2.4. Parameters for the material are set as follows: exchange coupling $H_J = 74$ T, Dzyaloshinskii-Moriya (DM) interaction $H_D = 2.07$ T, hard-axis anisotropy $H_K = 0.216$ T, and in-plane easy-axis anisotropy $H_A = 1.1 \times 10^{-3}$ T. This methodology leads to an estimated Gilbert damping coefficient of $\alpha \approx 4.6 \times 10^{-4}$, corroborated by experimental results.

Furthermore, the FWHM shows a marked increase at lower driving frequencies

before reaching a plateau as the frequency is increased. While this pattern is not overt within the current experimental frequency range, extending the driving frequency to approximately 100 GHz is expected to manifest this trend.

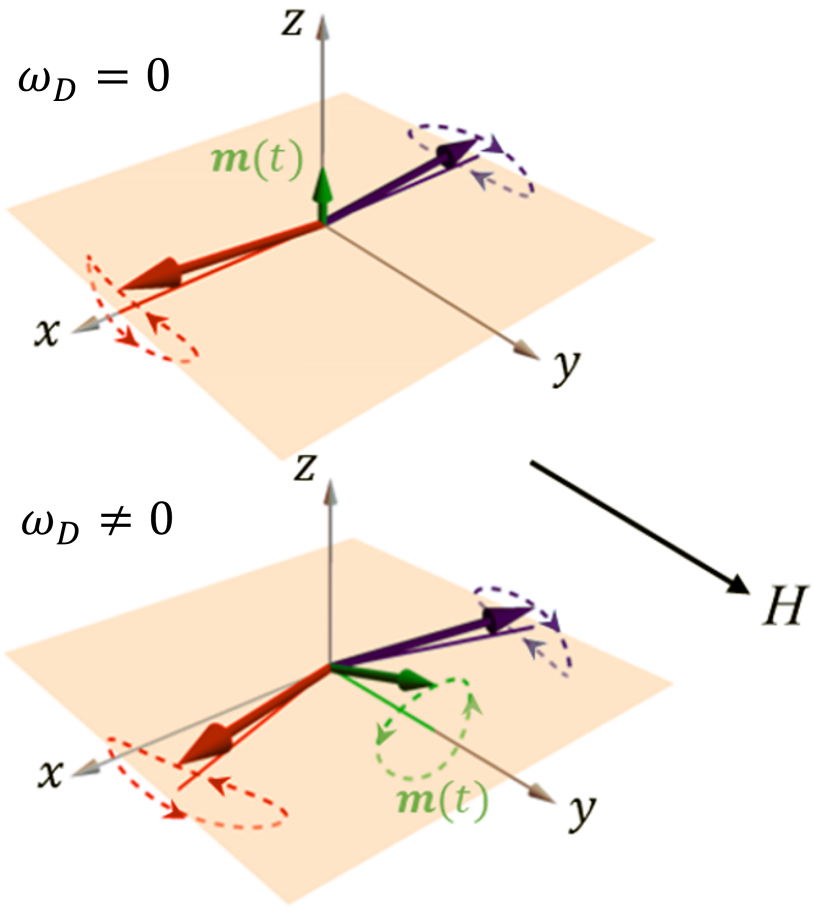

Figure 2.1: Schematic illustration of the mode in an easy-plane AFM with and without the DM field H_D. The external magnetic field H is applied along the y-axis. The solid green arrow which we labeled as $m(t)$ is the instantaneous magnetic moment while the dashed green curve illustrates the trajectory of $m(t)$

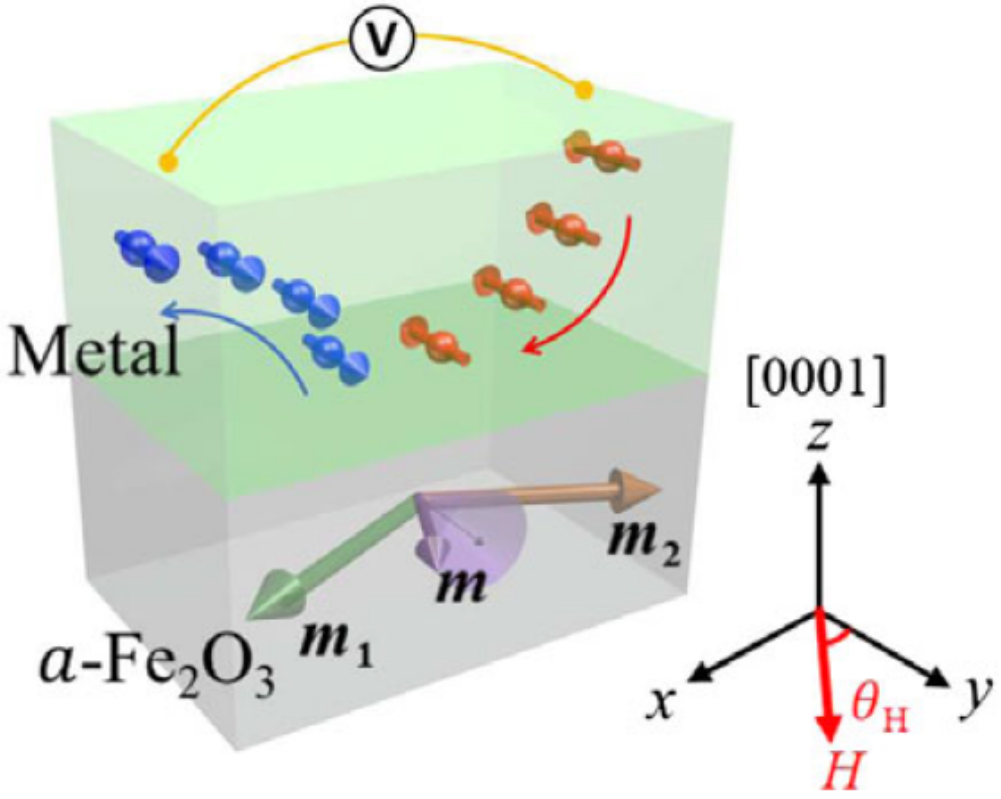

Figure 2.2: Schematic illustration depicts the dynamics of spin injection and the inverse spin Hall effect within an α-Fe_2O_3/metal heterostructure. The variables m_1 and m_2 denote the magnetic moments of the two antiferromagnetically coupled spin sublattices, while m represents the resultant canted ferromagnetic moment intrinsic to α-Fe_2O_3.

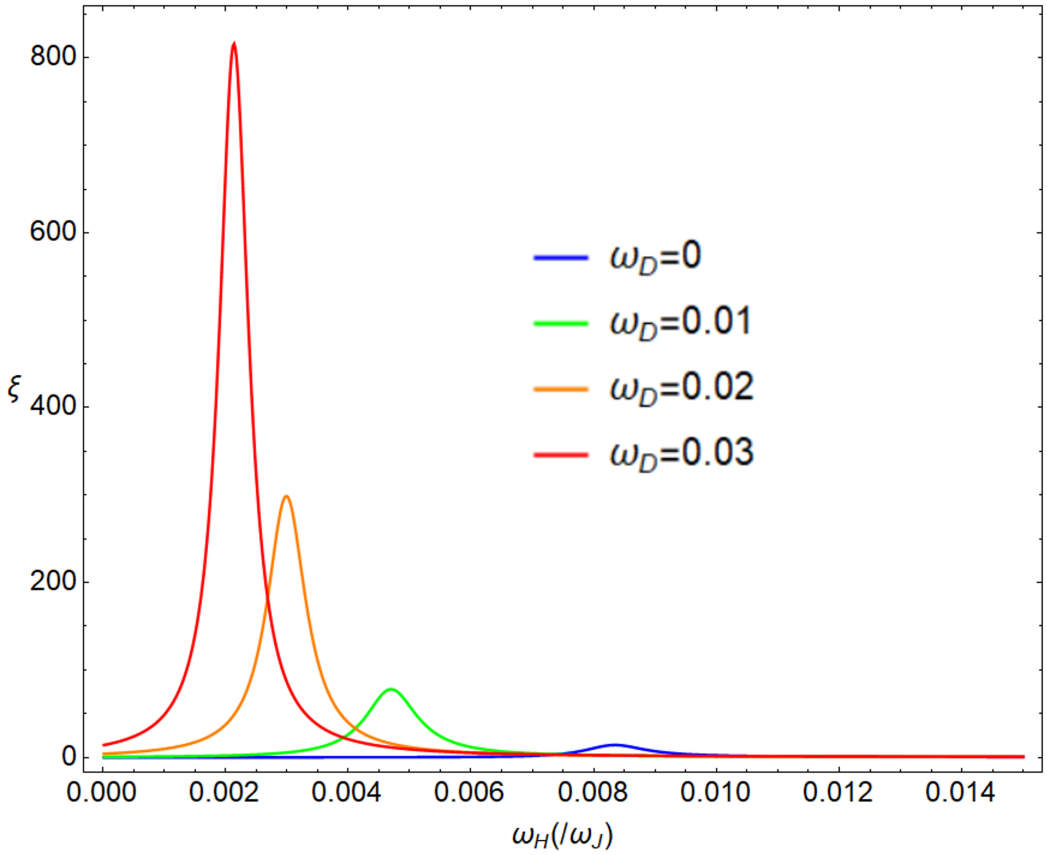

Figure 2.3: Figure demonstrates the calculated susceptibility of spin pumping, denoted as ξ, plotted against the external magnetic field ω_H. The calculation spans across a range of Dzyaloshinskii-Moriya (DM) fields, with $H_D^{\text{Max}} = 2.07 \times 10^4$ Oe representing the actual value obtained from measurements.

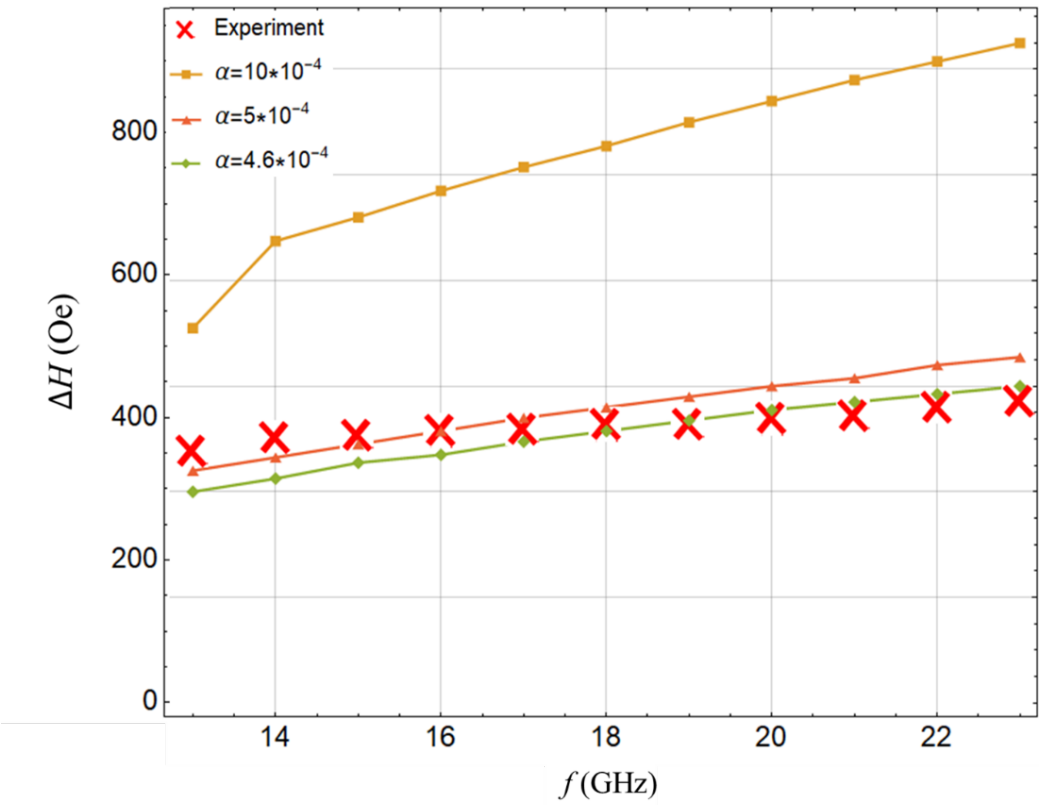

Figure 2.4: Calculated FWHM, ΔH, of the spin-pumping susceptibility, ξ, across the frequency range of 13 GHz to 23 GHz for three distinct Gilbert damping coefficients, α. The curve that corresponds to $\alpha = 4.6 \times 10^{-4}$ aligns optimally with the experimental data (denoted by red crosses), providing the most accurate representation of the observed spin-pumping phenomenon.

Chapter 3

Field-assisted Spin Pumping

In this chapter, we shift our focus from the non-collinear phase to the collinear phase, aiming to challenge the prevailing theories of spin pumping in NiO. Despite its popularity as an experimental antiferromagnetic material, NiO is often considered a poor candidate for spin-pumping applications. Our motivation stems from an in-depth analysis of NiO's eigenmodes below the spin-flop transition, which may reveal untapped potential in this material for spintronic applications.

3.1 Field-assisted Dynamics of NiO

We begin with a similar method mentioned in Chapter 2 by exploring a two-sublattice macrospin model where the antiferromagnetically coupled magnetic moments are represented by $\boldsymbol{M}_1$ and $\boldsymbol{M}_2$. The coordinate system is defined such that the easy-axis coincides with $\hat{\boldsymbol{x}}$, and the hard-axis with $\hat{\boldsymbol{z}}$, which situates the xy-plane as the easy plane. In the case of NiO, $\hat{\boldsymbol{z}}$ aligns with the (111) crystallographic direction, while $\hat{\boldsymbol{x}}$

corresponds to the $(11\bar{2})$ direction. The unit vectors $\boldsymbol{m}_1 = \boldsymbol{M}_1/M_s$ and $\boldsymbol{m}_2 = \boldsymbol{M}_2/M_s$ describe the orientations of the sublattice magnetic moments, with M_s being the saturation magnetization. The free energy density of NiO at low temperatures can be expressed using these vectors:

$$\epsilon = J\boldsymbol{m}_1 \cdot \boldsymbol{m}_2 - \frac{A}{2}\left[(\boldsymbol{m}_1 \cdot \hat{x})^2 + (\boldsymbol{m}_2 \cdot \hat{x})^2\right] + \frac{K}{2}\left[(\boldsymbol{m}_1 \cdot \hat{z})^2 + (\boldsymbol{m}_2 \cdot \hat{z})^2\right] - M_s\boldsymbol{H} \cdot (\boldsymbol{m}_1 + \boldsymbol{m}_2) \tag{3.1}$$

where $\boldsymbol{H}$ is the applied magnetic field, J, A, and K are the exchange coupling, the easy-axis and the hard-axis anisotropy, respectively, all being positive in our convention. The coherent dynamics of $\boldsymbol{m}_1$ and $\boldsymbol{m}_2$ is described by the LLG equations:

$$\begin{aligned}\dot{\boldsymbol{m}}_1 =& \omega_J \boldsymbol{m}_1 \times \boldsymbol{m}_2 - \omega_A \boldsymbol{m}_1 \times (\boldsymbol{m}_1 \cdot \hat{x})\hat{x} + \omega_K \boldsymbol{m}_1 \times (\boldsymbol{m}_1 \cdot \hat{z})\hat{z} \\ & - \omega_H \boldsymbol{m}_1 \times \hat{H} + \alpha \boldsymbol{m}_1 \times \dot{\boldsymbol{m}}_1, \end{aligned} \tag{3.2a}$$

$$\begin{aligned}\dot{\boldsymbol{m}}_2 =& \omega_J \boldsymbol{m}_2 \times \boldsymbol{m}_1 - \omega_A \boldsymbol{m}_2 \times (\boldsymbol{m}_2 \cdot \hat{x})\hat{x} + \omega_K \boldsymbol{m}_2 \times (\boldsymbol{m}_2 \cdot \hat{z})\hat{z} \\ & - \omega_H \boldsymbol{m}_2 \times \hat{H} + \alpha \boldsymbol{m}_2 \times \dot{\boldsymbol{m}}_2 \end{aligned} \tag{3.2b}$$

where $\hat{H}$ denotes the unit vector in the direction of the external magnetic field $\boldsymbol{H}$, and α is the Gilbert damping constant. The terms $\omega_J = J/\hbar$, $\omega_A = A/\hbar$, $\omega_K = K/\hbar$, and $\omega_H = HM_s/\hbar$ represent the angular frequencies associated with the exchange interaction, the anisotropy along the easy and hard axes, and the external magnetic field respectively, as they appear in the free energy equation (3.1).

For an external magnetic field $\boldsymbol{H}$ applied along the $\hat{x}$ direction (parallel to $\boldsymbol{m}_1$), we linearize LLG equations around the equilibrium configuration, $\boldsymbol{m}_{1,2} = \pm\hat{x}$, and determine the eigenfrequencies using the material parameters specific to NiO [42, 51]. As depicted in Figure 3.1(a), the eigenfrequencies of NiO exhibit a gap at zero field, which is ascribed to

the hard-axis anisotropy ω_K. The diagram reveals two distinct eigenfrequencies, referred to as acoustic and optical modes, which demonstrate a nonlinear yet continuous variation with an increasing magnetic field up to the spin-flop (SF) transition, demarcated by the dashed green line at approximately 7.8T.

In Figure 3.1(b), the polarization of each eigenvector is illustrated through the logarithm (base 10) of the ratio of the principal axes of the elliptical trajectories for $\boldsymbol{m}_1$ (red lines) and $\boldsymbol{m}_2$ (blue lines). Here, an unexpected divergence is observed at around 0.4T, significantly below the SF transition threshold. Specifically, in the acoustic mode (lower frequency), it is $\boldsymbol{m}_1$ that exhibits a diverging ratio ϵ_y/ϵ_z at this pivotal point, whereas the polarization of $\boldsymbol{m}_2$ in the optical mode (higher frequency) alters smoothly. This divergence highlights a critical behavior in the polarization dynamics of NiO under an external magnetic field, underscoring the complex interplay between anisotropy and magnetic field strength in determining the spin dynamics.

For comparison, we also examine the eigenfrequencies and polarization of the eigenmodes in the uniaxial AF MnF_2 [63, 46], as illustrated in Figures 3.1(c) and (d). On one hand, the two eigenfrequencies in MnF_2 are initially degenerate at zero field and then split linearly with an increasing magnetic field until the acoustic branch nearly approaches zero. On the other hand, both modes exhibit circular polarization below the SF transition, as indicated by $\lg(\epsilon_y/\epsilon_z) = 0$ [31]. This behavior contrasts with the observations in NiO, highlighting the distinct dynamics and polarization characteristics inherent to uniaxial antiferromagnets like MnF_2 under the influence of an external magnetic field.

3.2 Field-induced Chirality Flip

To elucidate the physical mechanisms underlying the unexpected divergence observed in Figure 3.1(b), we closely examine the vicinity of the critical point. Figure 3.1(e) schematically depicts the evolution of the precession trajectories of the two antiparallel magnetic moments. In the acoustic branch, both $\boldsymbol{m}_1$ and $\boldsymbol{m}_2$ exhibit elliptical rotation relative to the x-axis, with the major axis aligned along $\hat{y}$ and the minor axis along $\hat{z}$. Approaching the critical point, where $\epsilon_y/\epsilon_z \to \infty$, the trajectory of $\boldsymbol{m}_1$ narrows and subsequently reopens with reversed chirality, while $\boldsymbol{m}_2$'s chirality remains unchanged. The optical branch demonstrates a parallel trend, albeit with polarization changes occurring in the reverse manner. Based on the insights from Figure 3.1(e), we identify a significant range of magnetic field strengths between the critical point and the SF transition, where both magnetic moments process with identical chirality—a key condition for achieving nonzero DC spin pumping. Furthermore, we observe that the critical field H_c for the chirality flip exhibits a linear dependence on the hard-axis anisotropy ω_K, as illustrated in the inset of Figure 3.1(e). This finding underscores the pivotal role of hard-axis anisotropy in influencing the spin dynamics and chirality behaviors critical for spin-pumping processes.

Specifically, when the two magnetic moments process with opposite chirality, their contributions to DC spin pumping counteract each other, as the cross products $\boldsymbol{m}_1 \times \dot{\boldsymbol{m}}_1$ and $\boldsymbol{m}_2 \times \dot{\boldsymbol{m}}_2$ have opposing directions. [14]. Conversely, the generation of spin current becomes synergistic when both sublattice moments rotate congruently. Thus, the phenomenon of chirality flip, occurring below the SF transition, emerges as a pivotal mechanism for enabling DC spin pumping in NiO and analogous easy-plane AF materials, even within their collinear

phases. This field-induced chirality flip—a critical aspect previously neglected—mirrors the reestablishment of rotational symmetry around the easy axis, predominantly influenced by the Zeeman interaction. For instance, within the acoustic mode, the evolution of $\boldsymbol{m}_1$'s precession from one chirality to its antithesis serves to mitigate the energy cost imposed by escalating magnetic fields. The juncture at which this chirality conversion occurs, denoted by H_c, marks a critical threshold for the system's dynamic behavior and spin-pumping capabilities.

To further elucidate the concept of field-assisted spin pumping with a more visual approach, we delve into the behavior of the acoustic mode in NiO, as depicted in Fig. 3.2. Initially, in the absence of a magnetic field, as shown in Figure 3.2(a), the magnetic moments $\boldsymbol{m}_1$ (green) and $\boldsymbol{m}_2$ (purple) exhibit elliptical precession with opposing chirality. This dynamic leads to a linearly polarized Néel vector $\boldsymbol{n} = (\boldsymbol{m}_1 - \boldsymbol{m}_2)/2$ albeit with exaggerated trajectories for clearer illustration. Consequently, the resonance of $\boldsymbol{n}$ solely induces AC spin pumping, rendering the DC component effectively nonexistent—a challenge inherent to the broken rotational symmetry observed in bi-axial AF materials. Additionally, the cumulative magnetic moment $\boldsymbol{m} = (\boldsymbol{m}_1 + \boldsymbol{m}_2)/2$ exhibits linear oscillation along the z-axis, rendering it unresponsive to a driving microwave field $\boldsymbol{h}_{\mathrm{rf}}$ polarized along the y-axis and thereby incapable of activating the acoustic mode.

Transitioning to a scenario augmented by a Zeeman field, as illustrated in Figure 3.2(b), $\boldsymbol{m}_1$ undergoes a critical chirality flip at the specified critical point, which in turn fosters an elliptical precession of n. This alteration not only endows n with an elliptical trajectory but also induces a corresponding elliptical motion in the total moment

m, now featuring a notable projection onto the y-axis. Such a configuration permits effective coupling with, and activation by, the rf field, thereby facilitating detectable DC spin pumping.

3.3 Spin Pumping Signal

To further elucidate the discussed physical mechanism, we examine a Pt/NiO bilayer heterostructure, calculating the ISHE-induced voltage generated from coherent DC spin pumping. This calculation is performed under a constant driving frequency ω while the magnetic field H is varied along $\hat{x}$. Specifically, for ω within the frequency domain of the acoustic mode, the resonance field H_{res} is determined by the equation [42, 54, 53]:

$$H_{\text{res}} \approx \frac{\hbar}{M_s}\sqrt{2\omega_J\omega_A - \omega^2}, \tag{3.3}$$

This relation holds true within the exchange limit, where $\omega_A \ll \omega_K \ll \omega_J$. Based on the setup depicted in Figure 3.2 and discounting thermal excitations, such as the spin Seebeck effect, the ISHE voltage generated in the y-direction is given by:

$$V_{\text{sp}} = \omega \text{Im}\left[\chi^*_{yy}\chi_{zy}\right]\tilde{g}_r \frac{eL\rho\theta_{\text{SH}}}{2\pi}\frac{\lambda}{d_N}\tanh\left(\frac{d_N}{2\lambda}\right)|\boldsymbol{h}_{\text{rf}}|^2 \tag{3.4}$$

where $\chi_{ij} = \chi_{ij}(\omega, H_{\text{res}})$ (with i, j spanning y and z) denotes the dynamical susceptibility tensor. This tensor encapsulates the Néel vector's responsiveness to the microwave drive $\boldsymbol{h}_{\text{rf}}$, as expressed by:

$$n_i = \chi_{ij}(\omega, H_{\text{res}})h_{\text{rf},i}, \tag{3.5}$$

In the above equation, e represents the electron charge, and L, ρ, θ_{SH}, λ, and d_N specify the length, resistivity, spin Hall angle, spin diffusion length, and thickness of the Pt layer, re-

spectively. The term $\tilde{g}_r$, indicating the real part of the spin-mixing conductance, reflects the efficiency of spin transfer across the Pt/NiO interface. This efficiency is notably influenced by both the spin backflow effect and spin diffusion phenomena within the Pt layer [6, 25].

Figure 3.3 presents the numerical results derived from Eq. (3.4) for four distinct driving frequencies within the acoustic mode. Interestingly, a lower driving frequency corresponds to a more pronounced spin pumping signal occurring at a higher resonance field, aligning with the predictions of Eq. (3.3). As the resonance field H_{res} nears the SF transition threshold, the polarization of the sublattice magnetic moments—and consequently, that of $\boldsymbol{n}$—transitions towards a more circular profile, significantly bolstering the efficacy of DC spin pumping. Notably, at approximately 100 GHz, the spin pumping amplitude reaches magnitudes comparable to those observed in uniaxial AF materials. Highlighted in the inset is the ISHE voltage's dependency on the driving frequency, spanning from 90 GHz to 180 GHz—a frequency spectrum readily achievable with microwave technology.

3.4 Spin-torque Nano-oscillator

Given the capacity of a magnetic field to significantly offset the broken symmetry induced by bi-axial anisotropy, thereby facilitating substantial DC spin pumping even within the collinear phase, it is logical to anticipate a similar field-enhanced effect on the reciprocal phenomenon—specifically, the reduction in the current threshold required to initiate auto-oscillation of the Néel vector. To explore this, we incorporate the spin-transfer torque (STT), denoted as $\boldsymbol{\tau}_i = \boldsymbol{m}_i \times (\boldsymbol{\omega}_s \times \boldsymbol{m}_i)$, into Eq. (3.2). Here, $\boldsymbol{\omega}_s = \omega_s \hat{x}$, with ω_s representing the

STT strength, converted into the frequency domain as [11, 13]:

$$\omega_s = J_c \frac{\theta_{SH} e \rho \tilde{g}_r \lambda a^3}{\hbar d_{\mathrm{NiO}}}, \tag{3.6}$$

where J_c is the applied current density in the y direction, a and d_{NiO} are the lattice constant and thickness of the NiO layer. Considering the Néel vector $\boldsymbol{n}$ approximated as $\hat{x} + (n_y \hat{y} + n_z \hat{z})\mathrm{e}^{\mathrm{i}\omega t}$ and the magnetization $\boldsymbol{m}$ as $(m_y \hat{y} + m_z \hat{z})\mathrm{e}^{\mathrm{i}\omega t}$, where $n_{y,z} \ll 1$ and $m_{y,z} \ll 1$, we linearize the LLG equations with respect to the basis $\{m_y, m_z, n_y, n_z\}^{\mathrm{T}}$ to form an eigenvalue problem. The eigenfrequencies ω are then determined by the equation

$$\begin{vmatrix} \mathrm{i}\omega & \omega_H & \omega_s & \omega_K + \omega_A + \mathrm{i}\alpha\omega \\ -\omega_H & \mathrm{i}\omega & \omega_A + \mathrm{i}\alpha\omega & \omega_s \\ 0 & 2\omega_J + \omega_K + \omega_A & \mathrm{i}\omega & \omega_H \\ -2\omega_J - \omega_A & 0 & -\omega_H & \mathrm{i}\omega \end{vmatrix} = 0, \tag{3.7}$$

wherein only two of the four solutions are physically distinct, with the others being redundant. The two physical solutions, denoted as the acoustic mode ω_{ac} and the optical mode ω_{op}, in the context of STT interaction with Gilbert damping, yield complex values. The real parts of these solutions specify the precessional frequencies, while the imaginary parts delineate the stability of the eigenmodes. An eigenmode is considered unstable when its imaginary part $\mathrm{Im}[\omega]$ becomes zero, indicating the commencement of auto-oscillation.

Figures 3.4(a) and (b) illustrate the real and imaginary components of both modes as functions of the STT strength ω_s, for $\mu_0 H = 0$ T (black curves) and $\mu_0 H = 2$ T (red curves), applied parallel to $\boldsymbol{\omega}_s$. Notably, a magnetic field of 2 T exceeds the critical threshold, resulting in the Néel vector adopting left-handed chirality in ω_{ac}.

At $\mu_0 H = 0\mathrm{T}$, the real parts of the eigenfrequencies, $\mathrm{Re}[\omega_{\mathrm{ac}}]$ and $\mathrm{Re}[\omega_{\mathrm{op}}]$, converge as the STT strength increases, until they coalesce at a bifurcation point. Concurrently, the imaginary parts, $\mathrm{Im}[\omega_{\mathrm{ac}}]$ and $\mathrm{Im}[\omega_{\mathrm{op}}]$, remain degenerate and constant. Past this bifurcation point, $\mathrm{Im}[\omega_{\mathrm{ac}}]$ declines sharply, reaching zero at ②, a point just marginally beyond the bifurcation. According to Ref. [13], the anti-damping influence of STT is confined to the narrow interval between the bifurcation and ②, predominantly countervailing the hard-axis anisotropy's effects rather than directly opposing Gilbert damping.

Conversely, at $\mu_0 H = 2\mathrm{T}$, the dynamics alter significantly. The bifurcation point for the imaginary parts shifts to zero, rendering any STT application instantly antithetical to damping on the Néel vector, thus precipitating the auto-oscillation of the acoustic mode at the much-reduced threshold denoted by ①. Regarding the real parts, the Zeeman field obliterates the bifurcation point (effectively relocating it to infinity), ensuring the two modes never intersect. This field-induced phenomenon results in the bifurcation point's annulment, markedly lowering the threshold for auto-oscillation where $\mathrm{Im}[\omega_{\mathrm{ac}}] = 0$.

Upon elucidating the impact of the Zeeman field on the eigenfrequencies, it becomes pertinent to examine the eigenvectors for a more intuitive understanding of auto-oscillation dynamics. Particularly, we focus on the manner in which magnetic moments precess around their equilibrium directions at the auto-oscillation threshold (*i.e.*, $\mathrm{Im}[\omega_{\mathrm{ac}}] = 0$). We numerically simulate the eigenvectors at thresholds ① (for $\mu_0 H = 2\mathrm{T}$) and ② (for zero field), with Figures 3.4(c) and (d) displaying snapshots where amplitudes are exaggerated for clarity. Notably, both scenarios demonstrate left-handed chirality in the precession of sublattice magnetic moments. However, the orientation of the polarization plane, contain-

ing the major axis of elliptical trajectories and highlighted in green, varies significantly: it is nearly parallel to the easy plane of NiO at ① and inclined by approximately 45° at ②. This inclination at ② vividly illustrates the STT's counteraction against the hard-axis anisotropy [13].

It is crucial to recognize that the Zeeman field alone does not induce instability; rather, it is the anti-damping influence of STT that initiates auto-oscillation. Nonetheless, in the absence of magnetic fields, the hard-axis anisotropy of NiO significantly impedes the anti-damping effect. The Zeeman field contributes by mitigating the hard-axis anisotropy ω_K, thereby enhancing the STT's capability to counteract Gilbert damping and foster the anti-damping effect.

To elucidate the concept of field-assisted auto-oscillation further, we calculate the threshold STT ω_s^{th} as a function of the applied magnetic field for various Gilbert damping constants. Figure 3.4(e) demonstrates a monotonic decrease in ω_s^{th} with an increasing magnetic field, a trend that is particularly pronounced for lower Gilbert damping values. For instance, employing the experimental Gilbert damping value of $\alpha = 5\times10^{-4}$ [45], we find that a 6T magnetic field can reduce ω_s^{th} by over an order of magnitude (illustrated by the red curve). With an even smaller damping, say $\alpha = 1 \times 10^{-4}$, the reduction in ω_s^{th} approaches two orders of magnitude at 6T. Additionally, ω_s^{th} displays an asymmetric behavior with respect to H, with more significant reductions for positive H values (when the Zeeman field is parallel to the current-induced spin accumulation $\boldsymbol{\omega}_s$). This asymmetry is more distinctly captured in the output auto-oscillation frequency, as depicted in Figure 3.4(f). Specifically, positive (negative) magnetic fields parallel (antiparallel) to $\boldsymbol{\omega}_s$ favor the excitation of the

acoustic (optical) mode by STT. However, driving the optical mode into auto-oscillation (for negative H) destabilizes the system, leading to large-angle precession in the $y-z$ plane. Contrary to the STT threshold, the output frequency as a function of H remains nearly unaffected by α beyond 2T (1T) for positive (negative) magnetic fields, as demonstrated in Figure 3.4(f). This stability arises because the triggered auto-oscillation's output frequency primarily depends on the real part of the eigenfrequency, which is largely insensitive to Gilbert damping.

In the context of both spin pumping and spin-torque oscillation analyses, the application of a magnetic field in directions other than along the Néel vector reduces the overall effect due to two reasons: 1) It is the projection of the Zeeman field onto the Néel vector that influences the polarization of the eigenmodes; 2) Deviation of the Néel vector from the easy axis without a corresponding adjustment in $\boldsymbol{h}_{\mathrm{rf}}$ leads to diminished microwave absorption.

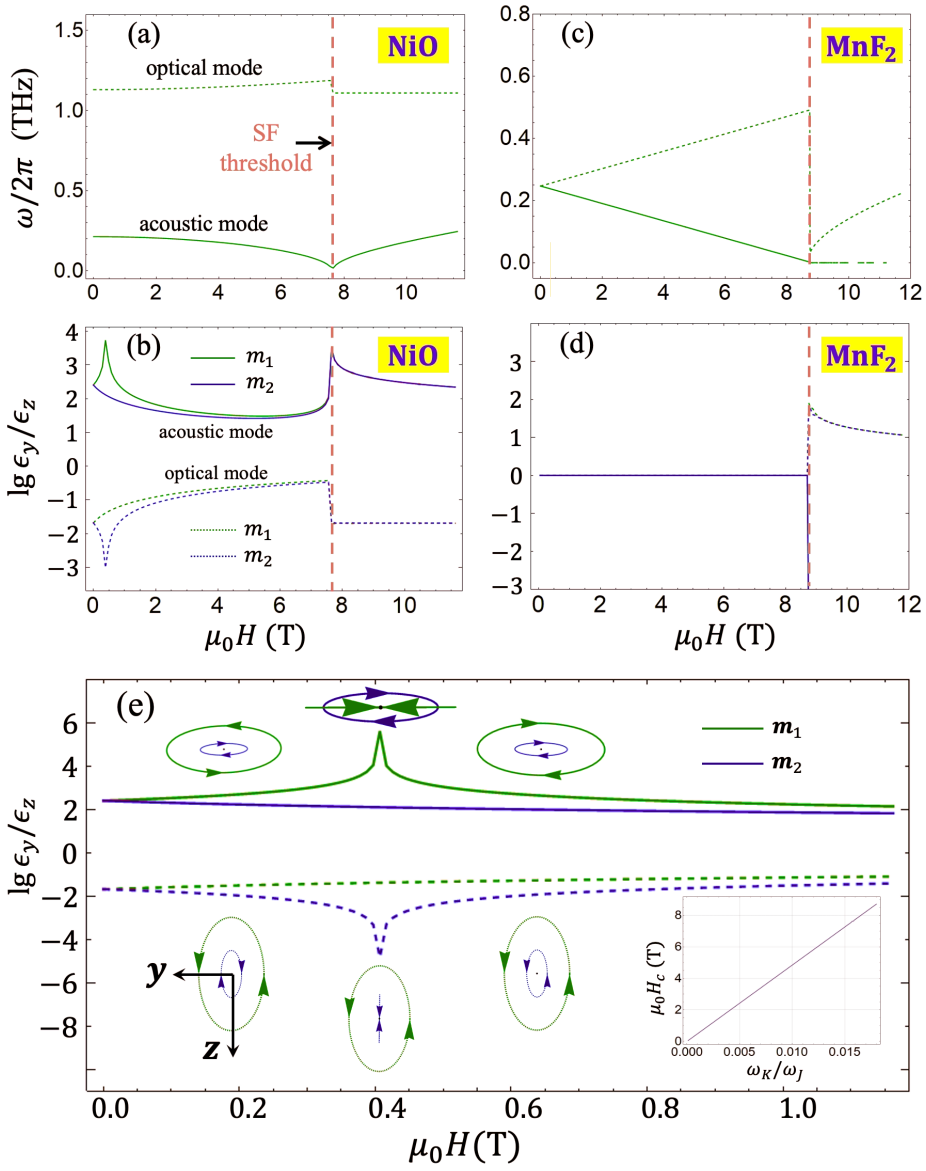

Figure 3.1: (a) eigenfrequencies and (b) polarization of the eigenmodes for NiO, compared with (c) and (d)—their counterparts in MnF_2. (e) Zoom-in plot of (b) in the vicinity of the critical point with illustrations of precession trajectories. Inset: dependence of the critical field on the hard-axis anisotropy. Parameters: for NiO, $\omega_J = 1.7 \times 10^{13}$, $\omega_K = 1.4 \times 10^{10}$, $\omega_A = 5.2 \times 10^8$ (rad/s), and $\alpha = 5 \times 10^{-4}$;

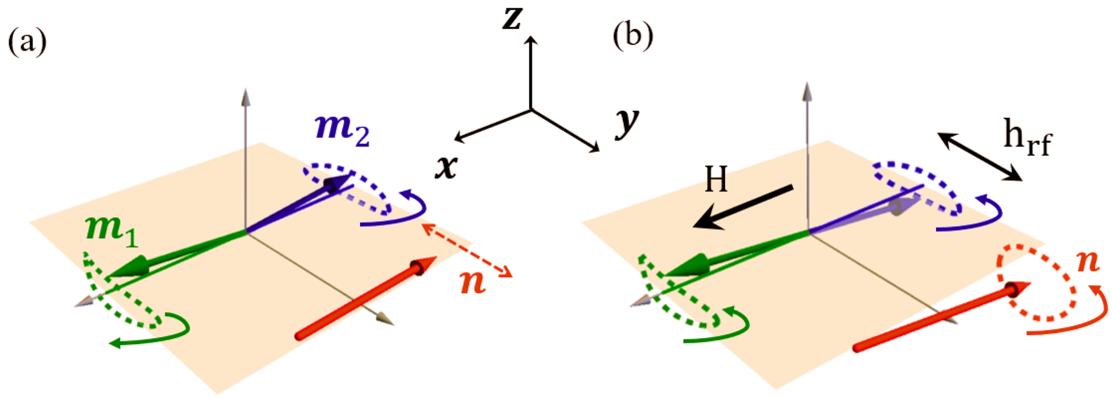

Figure 3.2: Figures (a) and (b) illustrate the acoustic mode in NiO at zero and non-zero magnetic fields, respectively, with an emphasis on the critical point where a chirality flip occurs. The depictions exaggerate the precession trajectories to enhance visual understanding. In (a), the absence of a magnetic field results in antiparallel precessions with opposite chirality, while in (b), the introduction of a magnetic field beyond the critical point induces a chirality flip, showcasing the altered dynamics.

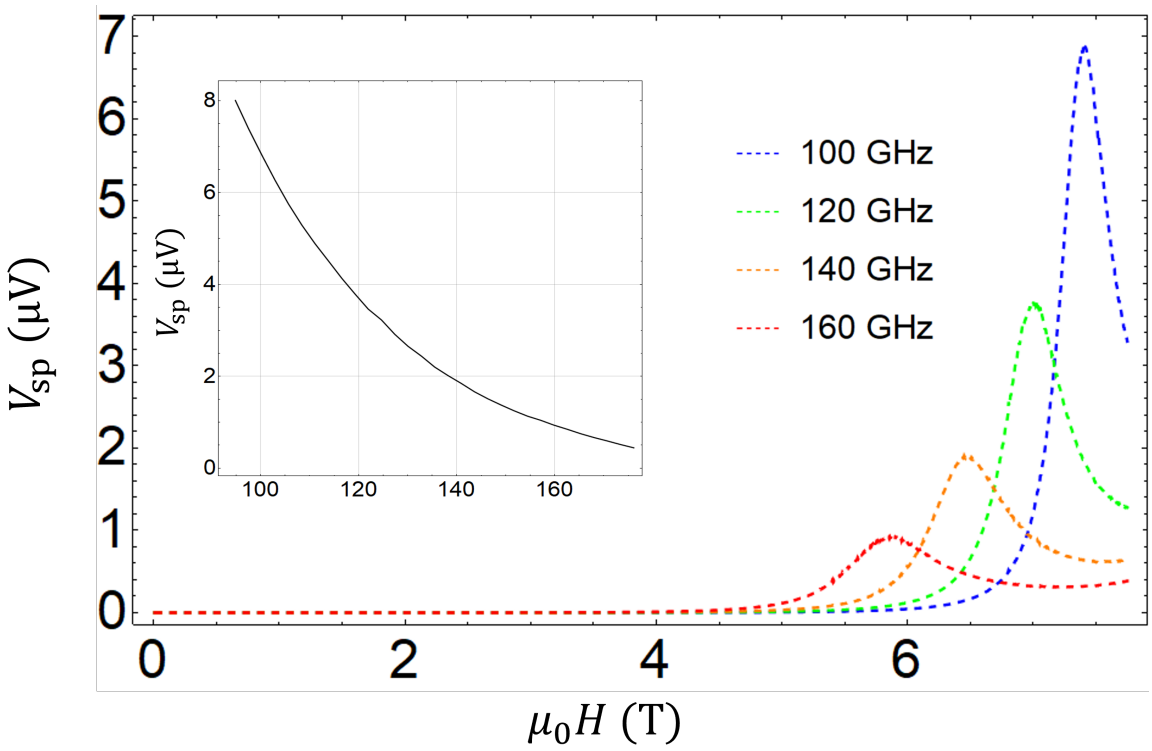

Figure 3.3: Strength of DC spin pumping as a function of the applied magnetic field at different driving frequencies in the acoustic branch. Inset: the output voltage varies with the driving frequency ranging from 90 to 180GHz.

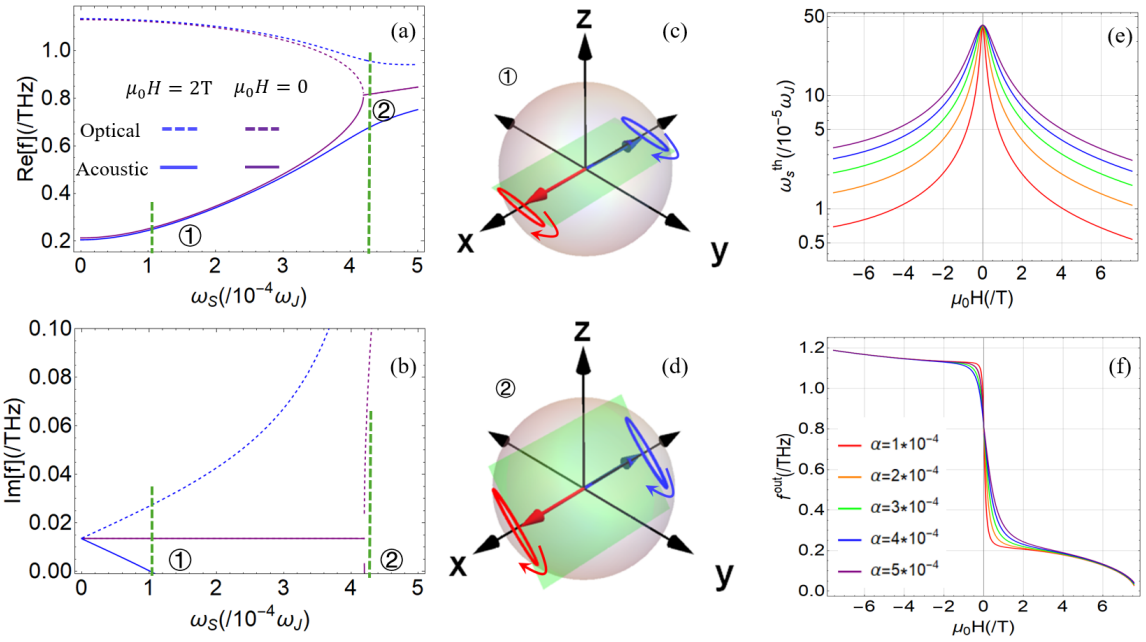

Figure 3.4: Figures (a) and (b) depict the real and imaginary components of the eigenfrequencies for NiO, respectively, as functions of the STT strength ω_s. The analyses are conducted for both zero magnetic field (black curves) and $\mu_0 H = 2\mathrm{T}$ (red curves). The STT thresholds in scenarios with (①) and without (②) an applied magnetic field are indicated. Notably, ② occurs just slightly above the bifurcation point. Panels (c) and (d) provide schematic representations of the eigenmodes at thresholds ① and ②, elucidating the system's behavior at these critical junctures. Finally, panels (e) and (f) illustrate the variations in STT threshold values and the resultant auto-oscillation output frequency as a function of the applied magnetic field, across different Gilbert damping constants.

Chapter 4

Spin Pumping in Ferrimagnets

4.1 From Antiferromagnets to Ferrimagnets

Although many advantages make AFM a good candidate for developing next-generation, multifunctional devices, there is still one intractable problem hindering the progress of AFM spintronics, and that is the vanishing magnetization. Despite the potential to manipulate AFM materials with extremely high currents, the lack of a net magnetization complicates the reading mechanisms in device engineering, rendering commercialization a formidable task[34].

A promising solution to this dilemma lies in the utilization of ferrimagnets (FIMs). FIMs exhibit magnetic moments that are antiparallel, akin to their AFM counterparts, yet they retain a remnant magnetization. This residual magnetization facilitates easier detection and manipulation of FIMs, making them more amenable to practical applications in spintronics. By leveraging the advantageous properties of FIMs, researchers can circumvent the challenges associated with the vanishing magnetization in AFMs, paving the way for

the development of more efficient and commercially viable spintronic devices.

FIMs hold the potential to function as high-frequency antiferromagnets while retaining the ease of detection characteristic of ferromagnets. This dual nature offers unprecedented opportunities for the development of ultrafast device applications, bridging the gap between the dynamic capabilities of antiferromagnets and the practical advantages of ferromagnets.

However, a comprehensive understanding of FIMs that encompasses the entire spectrum between the ferromagnetic and antiferromagnetic limits is still lacking. Developing such a generalized framework is crucial for unveiling unique characteristics that may not be apparent near the compensation points. Moreover, it would provide a unified perspective on the spin dynamics in FIMs, aligning them with those observed in purely ferromagnetic and antiferromagnetic materials. By exploring the full potential of FIMs, we can unlock new avenues for spintronic devices that leverage the best of both ferromagnetic and antiferromagnetic properties.

4.2 Static Properties

Considering a two-sublattice FIM characterized by macrospin variables $\boldsymbol{S}_1$ and $\boldsymbol{S}_2$ that are antiferromagnetically coupled. The corresponding sublattice magnetic moments are $\boldsymbol{M}_1 = \gamma_1 \boldsymbol{S}_1$ and $\boldsymbol{M}_2 = \gamma_2 \boldsymbol{S}_2$, where the gyromagnetic ratios γ_1 and γ_2 may generally differ. This disparity in magnetizations leads to a competition that switches at the temperature of angular momentum compensation [36, 56]. However, in typical FIMs composed of Fe, Co, and Gd ions, γ_1 and γ_2 differ by only a few percent. Thus, for simplicity, assume

$\gamma_1 = \gamma_2 = \gamma$, capturing the essential behavior of FIMs. Consequently, the ratio of sublattice spins and magnetizations can be represented by the same parameter $\xi = |S_2/S_1| = |M_2/M_1|$. The total spin $S = |S_1| + |S_2|$ remains constant, implying that the total magnetic moment $M_s \equiv \gamma S = |M_1| + |M_2|$ is also constant. Accordingly:

$$\frac{|M_1|}{M_s} = \frac{1}{\xi + 1}, \tag{4.1a}$$

$$\frac{|M_2|}{M_s} = \frac{\xi}{\xi + 1}. \tag{4.1b}$$

The parameter ξ can continuously vary from 0 to 1. When $\xi \to 0$, one sublattice vanishes, and the system effectively behaves as a ferromagnetic material. Conversely, when $\xi \to 1$, the two sublattices fully compensate, rendering the system antiferromagnetic. The broad range of ξ encompasses a wide variety of FIMs with different chemical compositions and allows exploration of physically interesting regions beyond the reach of temperature variations, uncovering profound implications not necessarily achievable in real materials.

By analyzing the ground state using two dimensionless vectors $\boldsymbol{m}_1 = \boldsymbol{M}_1/M_s$ and $\boldsymbol{m}_2 = \boldsymbol{M}_2/M_s$ (note: these are *not* unit vectors). The free energy density is given by:

$$\begin{aligned}\epsilon =& J\boldsymbol{m}_1 \cdot \boldsymbol{m}_2 - \frac{A}{2}[(\boldsymbol{m}_1 \cdot \hat{x})^2 + (\boldsymbol{m}_2 \cdot \hat{x})^2] \\ &+ \frac{K}{2}[(\boldsymbol{m}_1 \cdot \hat{z})^2 + (\boldsymbol{m}_2 \cdot \hat{z})^2] - M_s \boldsymbol{H}_0 \cdot (\boldsymbol{m}_1 + \boldsymbol{m}_2),\end{aligned} \tag{4.2}$$

where $\boldsymbol{H}_0$ is the external magnetic field, and J, A, and K represent the antiferromagnetic (AFM) exchange coupling, easy-axis, and hard-axis anisotropy, respectively. These constants are taken to be positive and have absorbed the factor of S. Given the difficulty in deriving sublattice-specific anisotropy forms in FIMs and their lack of universality, a common simplification that treats the anisotropy energies for both sublattices equally [35, 33]

can be adopted. Additionally, due to the typical dominance of K over A, inducing an out-of-plane rotation necessitates an impractically large magnetic field. Thus, in-plane fields are focused on, parameterized by the azimuthal angle ϕ, as depicted in Fig. 4.1(a). As ϕ varies, $\boldsymbol{m}_1$ and $\boldsymbol{m}_2$ undergo in-plane rotations characterized by angles θ_1 and θ_2, respectively. This allows us to express the free energy density ϵ as a function of three angles:

$$\begin{aligned}\epsilon =& \frac{\hbar\xi}{(\xi+1)^2}\left[\omega_J\cos(\theta_1-\theta_2)-\frac{\omega_A}{2}(\cos^2\theta_1+\xi^2\cos^2\theta_2)\right] \\ &-\frac{\hbar\omega_H}{\xi+1}[\cos(\phi-\theta_1)+\xi\cos(\phi-\theta_2)],\end{aligned} \tag{4.3}$$

where $\hbar\omega_J = J$, $\hbar\omega_A = A$, $\hbar\omega_H = H_0 M_s$, and a constant term proportional to K has been omitted. The equilibrium state is obtained by minimizing ϵ with respect to θ_1 and θ_2 under given field strength ω_H and field angle ϕ. For convenience in simulating spin dynamics, all parameters are scaled into angular frequencies, and we set $\omega_J = 1$ so that ω_A and ω_H are normalized to the exchange energy.

Before exploring variations in ξ, the system's response to an increasing magnetic field and its distinction from the antiferromagnetic (AFM) case for a specific value of $\xi = 0.5$ (i.e., $S_2 = S_1/2$) are examined firstly. Figure 4.1(b) illustrates the angles θ_1 and θ_2 as functions of the field strength ω_H at various field angles. When $\phi = 0$, meaning that $\boldsymbol{H}_0$ is aligned with the easy axis, the two spins remain unchanged until a spin-flop (SF) transition occurs around $\omega_H = 0.4$. At this point, they abruptly rotate towards a canted configuration. Beyond the SF transition, the spins increasingly align with the field direction until full polarization is achieved at approximately $\omega_H = 0.95$, marking the onset of the spin-flip phase [3]. This behavior closely resembles that observed in AFM systems. However, a

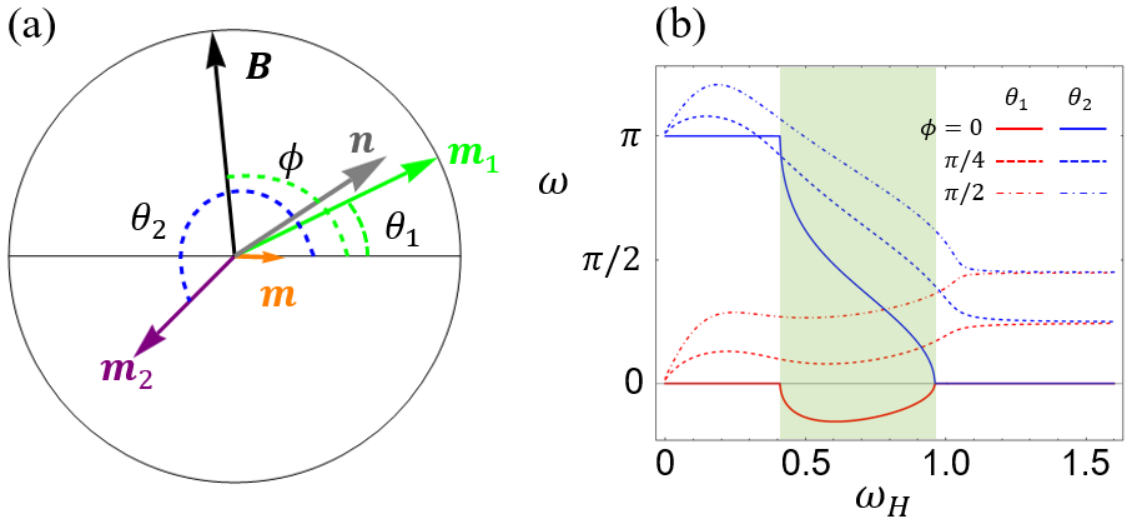

Figure 4.1: (a) Schematic illustration of system geometry. The vectors $\boldsymbol{m}_1$, $\boldsymbol{m}_2$, and $\boldsymbol{B}$ are characterized by θ_1, θ_2, and ϕ relative to the positive $\hat{x}$ direction. The unit vector of total magnetization $\boldsymbol{m} = (\boldsymbol{m}_1 + \boldsymbol{m}_2)/2$ and the Néel vector $\boldsymbol{n} = (\boldsymbol{m}_1 - \boldsymbol{m}_2)/2$ are represented by orange and purple arrows. (b) θ_1 (red) and θ_2 (blue) as functions of the field strength ω_H along different field angle ϕ, where a SF phase (shaded) is clearly seen for $\phi = 0$. (c)-(f) The perpendicular and parallel components of $\boldsymbol{m}$ and $\boldsymbol{n}$ with respect to the field direction when ϕ varies from 0 to 2π at different field strengths. Orange and blue curves are below the SF transition, red curves are within the SF phase, and green curves are in the spin-flip phase. $\xi = 0.5$ and $\omega_A = 0.08$ are used for all plots.

notable difference is that θ_1 and θ_2 are continuous across the entire range, including the SF transition, whereas in the AFM limit, they both exhibit a near $\pi/2$ jump at the SF point. For non-zero field angles, the SF phase boundaries become blurred, resulting in continuous changes in both θ_1 and θ_2, as well as their derivatives with respect to ω_H.

Subsequently, the ground state configuration by varying the field angle ϕ continuously from 0 to 2π are explored. Figures 4.2(a)-4.2(d) present the absolute values of the parallel and perpendicular components of $\boldsymbol{m} = (\boldsymbol{m}_1 + \boldsymbol{m}_2)/2$ and $\boldsymbol{n} = (\boldsymbol{m}_1 - \boldsymbol{m}_2)/2$ relative to the field direction as functions of ϕ for four distinct field strengths: two below the spin-flop (SF) transition, one within the SF phase, and one in the spin-flip phase. While the parallel components $\boldsymbol{m}_\parallel$ and $\boldsymbol{n}_\parallel$ exhibit minimal variation with ϕ, the perpendicular components $\boldsymbol{m}_\perp$ and $\boldsymbol{n}_\perp$ display characteristic patterns in different phases: two lobes in the collinear phase, a single lobe in the SF phase, and four diminutive lobes in the spin-flip phase. Notably, irrespective of the field strength, all components exhibit periodic behavior, repeating themselves in the intervals $\phi \in [0, \pi]$ and $\phi \in [\pi, 2\pi]$. Therefore, for subsequent analyses, we will focus solely on the range $\phi \in [0, \pi]$.

To gain deeper insights into the equilibrium properties, the perpendicular component $\boldsymbol{m}_\perp$ should be concentrated on, where the spin-flop (SF) phase is more pronounced. Figure 4.3 expands upon Figure 4.2(c) to cover arbitrary field strengths ω_H for different values of ξ. The horizontal and vertical cuts in the specific case of $\xi = 0.5$ correspond to the curves depicted in Figure 4.2(b) and Figures 4.2(c)-4.2(f), respectively. It is evident that the SF phase is delimited by an ear-shaped contour near $\phi = 0$ and π, which expands (contracts) with increasing (decreasing) ξ. For $\xi = 0.1$, the SF phase is nearly indiscernible.

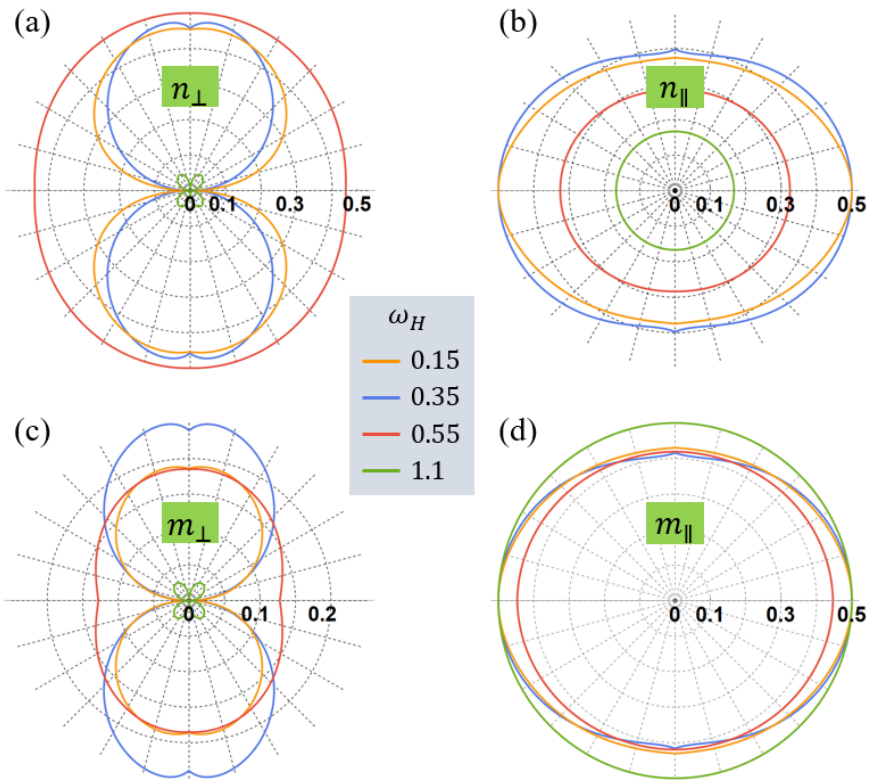

Figure 4.2: (a)-(d) The perpendicular and parallel components of $\boldsymbol{m}$ and $\boldsymbol{n}$ with respect to the field direction when ϕ varies from 0 to 2π at different field strengths. Orange and blue curves are below the SF transition, red curves are within the SF phase, and green curves are in the spin-flip phase. $\xi = 0.5$ and $\omega_A = 0.08$ are used for all plots.

As the ferromagnetic (FM) limit $\xi \to 0$ is approached (not shown), the SF phase vanishes entirely. The variation of ξ showcased in Figure 4.3 intuitively illustrates how ferrimagnets (FIMs) inherently bridge their FM and antiferromagnetic (AFM) limits at equilibrium.

4.3 Dynamical Properties

With the equilibrium spin configuration of the model FIM established, attention shifts to the dynamical eigenmodes, specifically how magnetic moments precess around their equilibrium positions. While determining the ground state can be simplified to a two-dimensional problem when the external magnetic field $\boldsymbol{H}_0$ is confined to the easy plane, dynamical properties are inherently three-dimensional due to the unavoidable out-of-plane motions involved in spin precessions. The presence of a magnetic field can induce non-collinearity between $\boldsymbol{m}_1$ and $\boldsymbol{m}_2$. Therefore, two local coordinate frames are introduced to describe their dynamical precessions around their individual equilibrium positions [69, 44], as schematically illustrated in Figure 4.4(a). Under this geometry, the free energy in

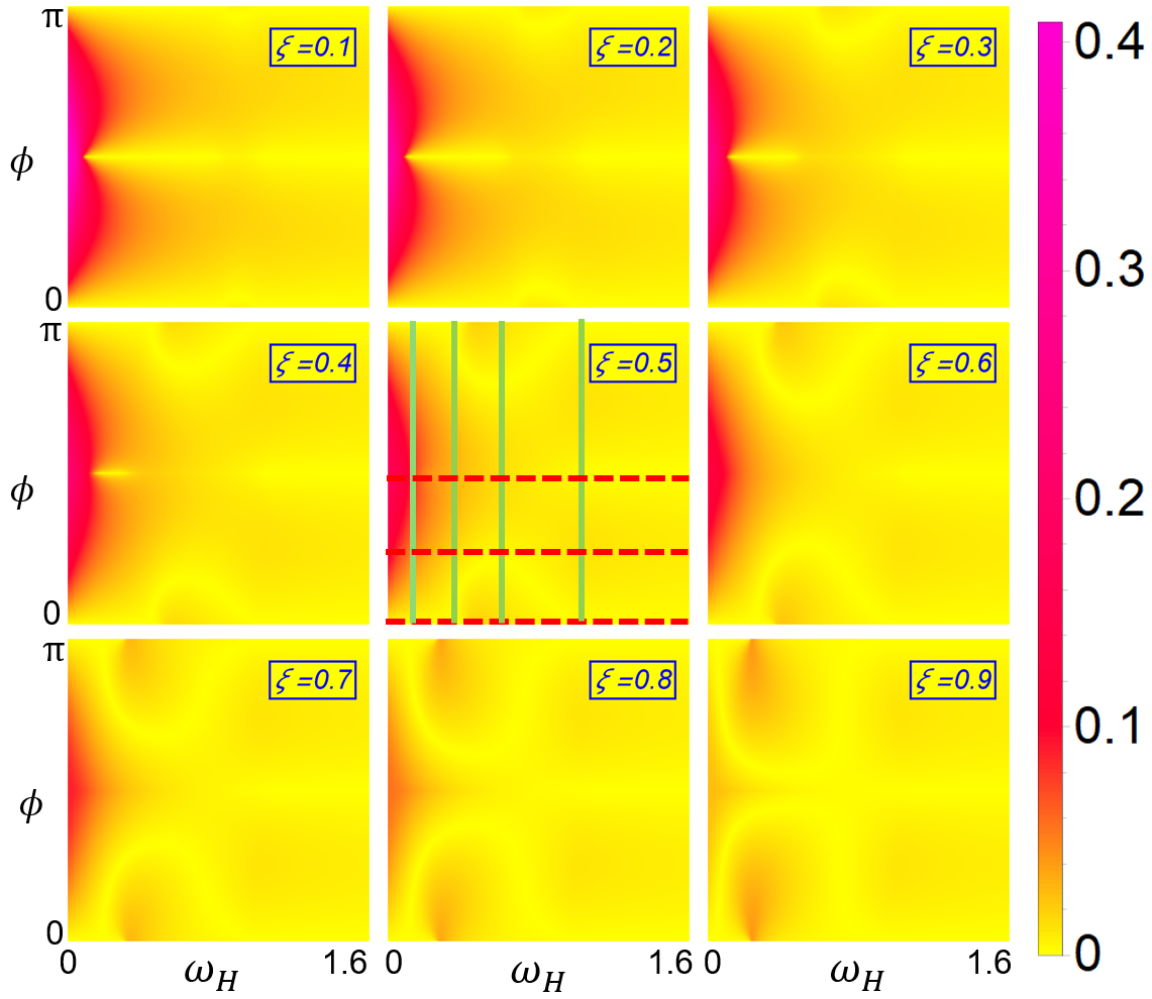

Figure 4.3: Density plot of $|m_\perp|$ as a function of ω_H (relative to ω_J) and ϕ for nine different values of ξ. For $\xi = 0.5$, the red and the green cuts correspond to the curves plotted in Fig. 4.1(b) and Figs. 4.2(a)-4.2(d), respectively. The SF phase is enclosed by an ear-shaped contour near $\phi = 0$ and π, which expands (shrinks) with an increasing (decreasing) ξ towards the AFM (FM) limit.

Eq. (4.3) can be reformulated as:

$$\begin{aligned}
\epsilon = & \frac{\hbar\omega_J\xi}{(\xi+1)^2}\left[Z_1Z_2 + (X_1X_2 + Y_1Y_2)\cos(\theta_1-\theta_2)\right. \\
& \left.+(X_1Y_2 - Y_1X_2)\sin(\theta_1-\theta_2)\right] + \frac{\hbar\omega_K}{2(\xi+1)^2}(Z_1^2 + \xi^2 Z_2^2) \\
& - \frac{\hbar\omega_A}{2(\xi+1)^2}\left[X_1\cos^2\theta_1 + Y_1\sin^2\theta_1\right. \\
& \quad + \xi^2(X_2\cos^2\theta_2 + Y_2\sin^2\theta_2^2) \\
& \quad \left.-2(X_1Y_1\cos\theta_1\sin\theta_1 + \xi^2 X_2Y_2\cos\theta_2\sin\theta_2)\right] \\
& - \frac{\hbar\omega_H}{\xi+1}\left[X_1^2\cos(\phi-\theta_1) + \xi X_2^2\cos(\phi-\theta_2)\right. \\
& \quad \left.-Y_1^2\sin(\phi-\theta_1) + \xi Y_2^2\sin(\phi-\theta_2)\right], \qquad (4.4)
\end{aligned}$$

where X_i, Y_i, and Z_i represent the components of $\boldsymbol{m}_i$ $(i = 1, 2)$ normalized in their respective local coordinate frames. By expressing the Landau-Lifshitz-Gilbert (LLG) equation $\dot{\boldsymbol{m}}_i = \boldsymbol{f}_i \times \boldsymbol{m}_i$ with $\boldsymbol{f}_i = -\frac{\delta\epsilon}{\hbar\delta\boldsymbol{m}_i}$ in terms of X_i, Y_i, and Z_i, we can linearize the spin dynamics to determine the eigenfrequencies and eigenmodes. While the inclusion of Gilbert damping $\alpha\boldsymbol{m}_i \times \dot{\boldsymbol{m}}_i$ leads to a slight frequency shift, the fundamental characteristics of the spectrum remain intact. Therefore, for the sake of simplicity, we neglect the damping effect in this section.

The analysis commences with a simple case where the hard-axis anisotropy is negligible ($\omega_K = 0$) and the external magnetic field $\boldsymbol{H}_0$ is aligned along the easy axis ($\phi = 0$). Under these conditions, the system exhibits rotational symmetry around the easy axis, leading to a collinear ground state. Similar to collinear antiferromagnets (AFMs), this symmetry gives rise to two circularly polarized modes with eigenfrequencies (in the

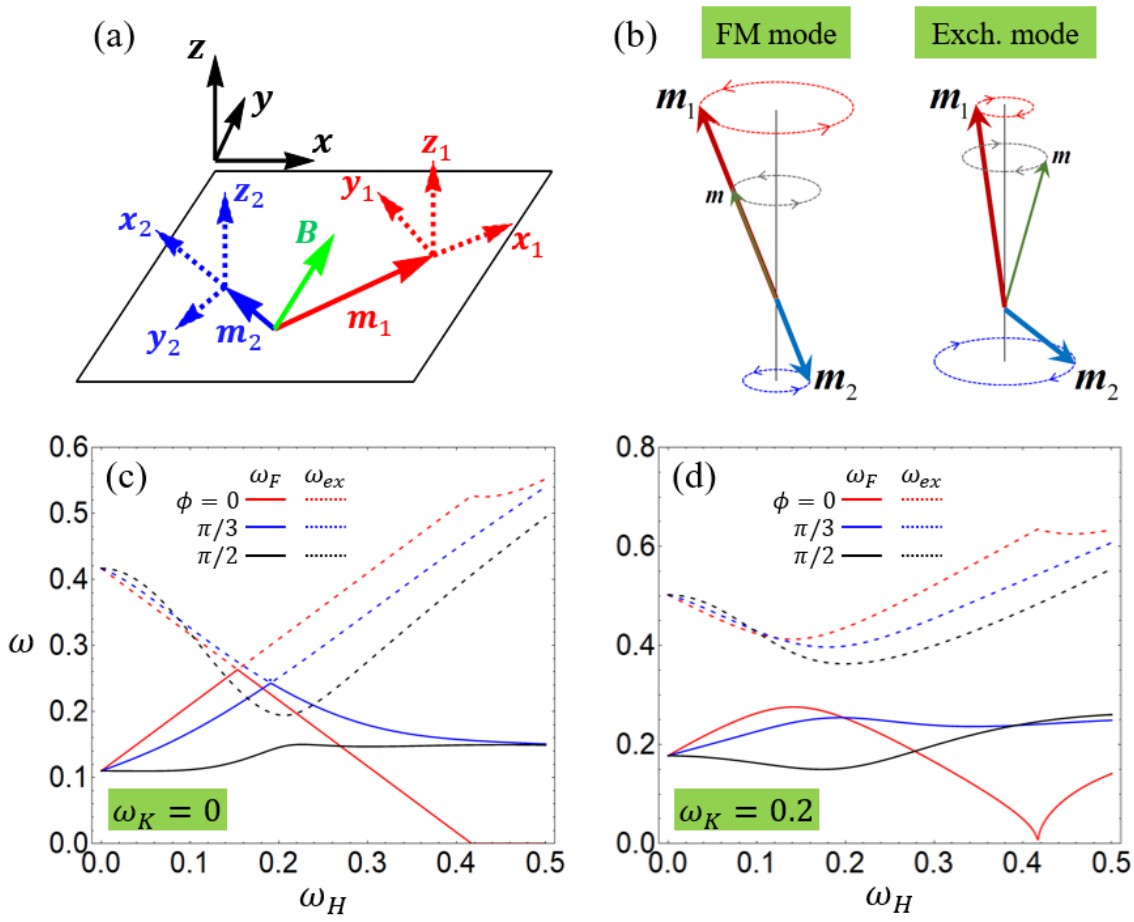

Figure 4.4: (a) Schematics of the model FIM in the presence of an in-plane magnetic field, where two local coordinates are defined based on the equilibrium orientations of $\boldsymbol{m}_1$ and $\boldsymbol{m}_2$. (b) Illustration of the two circularly-polarized eigenmodes in an easy-axis FIM ($\omega_K = 0$) when $\boldsymbol{H}_0$ is applied along $\hat{x}$. Panels(c) and (d) plot the two eigenfrequencies as functions of the applied field along three different directions for easy-axis and easy-plane FIM, respectively, for $\xi = 0.5$ (or $\beta = 1/3$) and $\omega_A = 0.08$. The FM mode (solid curves) and the exchange mode (dashed curves) become degenerate at a critical field below the SF threshold if and only if $\omega_K = 0$ and $\phi = 0$. Either a finite hard-axis anisotropy ω_K or a nonzero field angle ϕ (or both) will lift the degeneracy.

exchange approximation $\omega_A \ll \omega_J$) given by:

$$\omega_F = \frac{\sqrt{\omega_A^2 + 2\omega_J\omega_A + \beta^2\omega_J^2}}{2} - \frac{\beta}{2}(\omega_J - \omega_A) + \omega_H, \tag{4.5a}$$

$$\omega_{ex} = \frac{\sqrt{\omega_A^2 + 2\omega_J\omega_A + \beta^2\omega_J^2}}{2} + \frac{\beta}{2}(\omega_J - \omega_A) - \omega_H, \tag{4.5b}$$

where the subscript "F" ("ex") denotes the ferromagnetic (FM) (exchange) mode, typically in the GHz (sub-THz) regime. The parameter $\beta \equiv \frac{1-\xi}{1+\xi}$ ranges from 0 (AFM limit) to 1 (FM limit). In the AFM limit $\beta \to 0$ (or $\xi \to 1$), the eigenfrequencies reduce to $\omega_\pm = \sqrt{\omega_A^2 + 2\omega_J\omega_A}/2 \pm \omega_H$, consistent with Kittel's formula for AFM materials. Conversely, in the FM limit $\beta \to 1$ (or $\xi \to 0$), the eigenfrequencies become $\omega_F = \omega_H$ and $\omega_{ex} = \omega_J - \omega_H$ if $\omega_A \to 0$.

When the magnetic field deviates from the easy axis, the rotational symmetry is disrupted, leading to a hybridization of the two circularly polarized modes as their eigenfrequencies converge. This interaction results in an avoided crossing, as depicted by the blue and black curves in Fig. 4.4(c). Furthermore, a finite hard-axis anisotropy ω_K can significantly widen this anti-crossing gap, as it also disrupts the rotational symmetry, as shown in Fig. 4.4(d).

To elucidate the hybridization of chiral eigenmodes in the absence of rotational symmetry, the vicinity of the anti-crossing gap is examined in detail, revealing the evolution of chirality for each magnetic moment in their respective local frames. Figures 4.5(a) and 4.5(b) illustrate this behavior. In the ferromagnetic (FM) mode, the chirality of $\boldsymbol{m}_1$ flips as the magnetic field crosses point ④, delineating regions of opposite chirality. Similarly, $\boldsymbol{m}_2$ undergoes a chirality flip at point ②. Conversely, in the exchange mode, $\boldsymbol{m}_1$

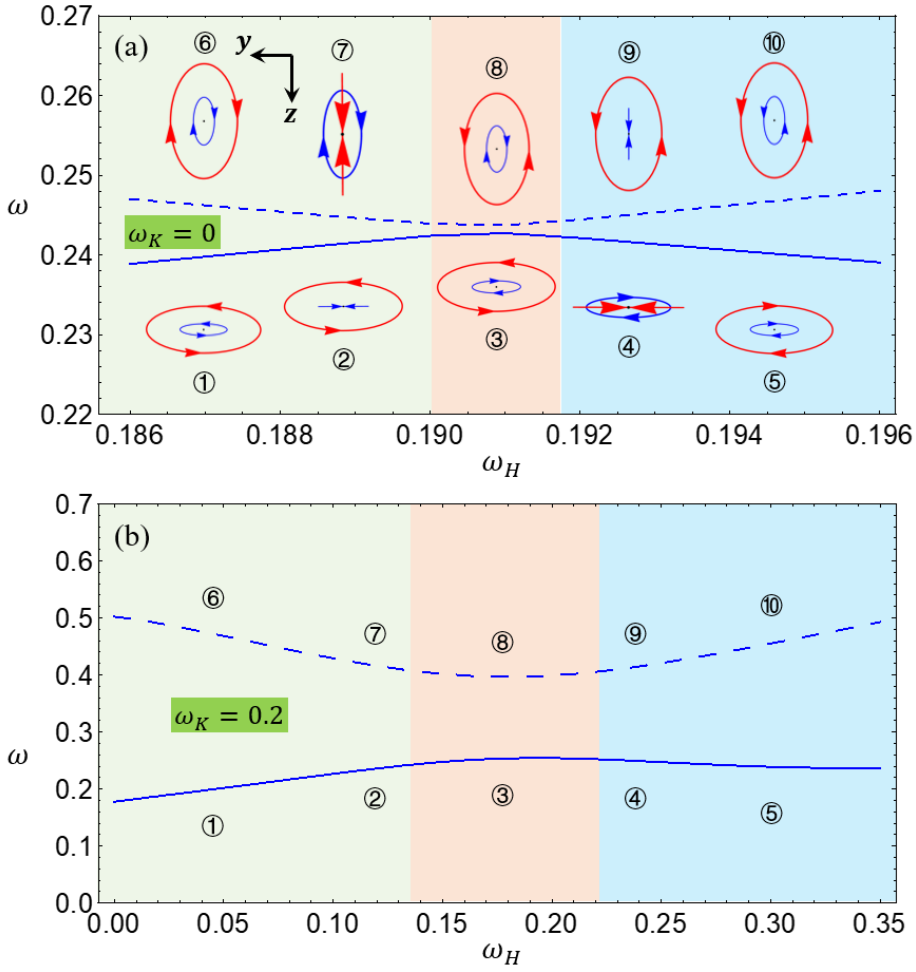

Figure 4.5: (a) and (b) are zoom-in plots of the avoided crossing corresponding to (c) and (d) for $\phi = \pi/3$, respectively. Here, the chirality of $\boldsymbol{m}_1$ ($\boldsymbol{m}_2$) is illustrated by red (blue) ellipses as seen from the $+x_1$ ($-x_2$) direction. In the FM mode, $\boldsymbol{m}_1$ ($\boldsymbol{m}_2$) becomes linearly polarized when the magnetic field reaches point ④ (②), across which $\boldsymbol{m}_1$ ($\boldsymbol{m}_2$) flips its chirality of precession. The ④ and ② points separate regions of distinct elliptical precessions colored differently. The exchange mode follows a somewhat reversed pattern, which is marked by ⑥ to ⑩.

experiences a chirality flip first, followed by $\boldsymbol{m}_2$ as the magnetic field strength increases. The presence of a hard-axis anisotropy ω_K not only enlarges the anti-crossing gap but also extends the range where the two magnetic moments exhibit opposite chirality. This effect is denoted by ③ for the FM mode and ⑧ for the exchange mode. The interplay between the magnetic field and anisotropy thus plays a crucial role in dictating the chiral dynamics of the magnetic moments in ferrimagnetic systems.

The influence of the central parameter in our model, ξ, on the eigenmodes is examined in the final analysis. Figure 4.6(a) displays the two eigenfrequencies as functions of a sweeping magnetic field along various in-plane directions for $\xi = 0.2$, 0.5, and 0.8. For the case of $\xi = 0.5$, the collinear, spin-flop (SF), and spin-flip phases are color-coded for clarity. In Figure 4.6(b), the polarization of each sublattice magnetic moment is characterized by the ratio of principal axes of the elliptical trajectory in the local frame, ϵ_y/ϵ_z, for $\phi = \pi/3$ at the three corresponding values of ξ. The points of divergence (zero) correspond to locations where the magnetic moment becomes linearly polarized along the in-plane Y (out-of-plane Z) direction in the local frame. As the field range extends significantly higher than in Figure 4.4, an additional chirality flip occurring within the SF phase is revealed, further illustrating the complex interplay between the magnetic field, anisotropy, and the parameter ξ in shaping the dynamical behavior of ferrimagnetic systems.

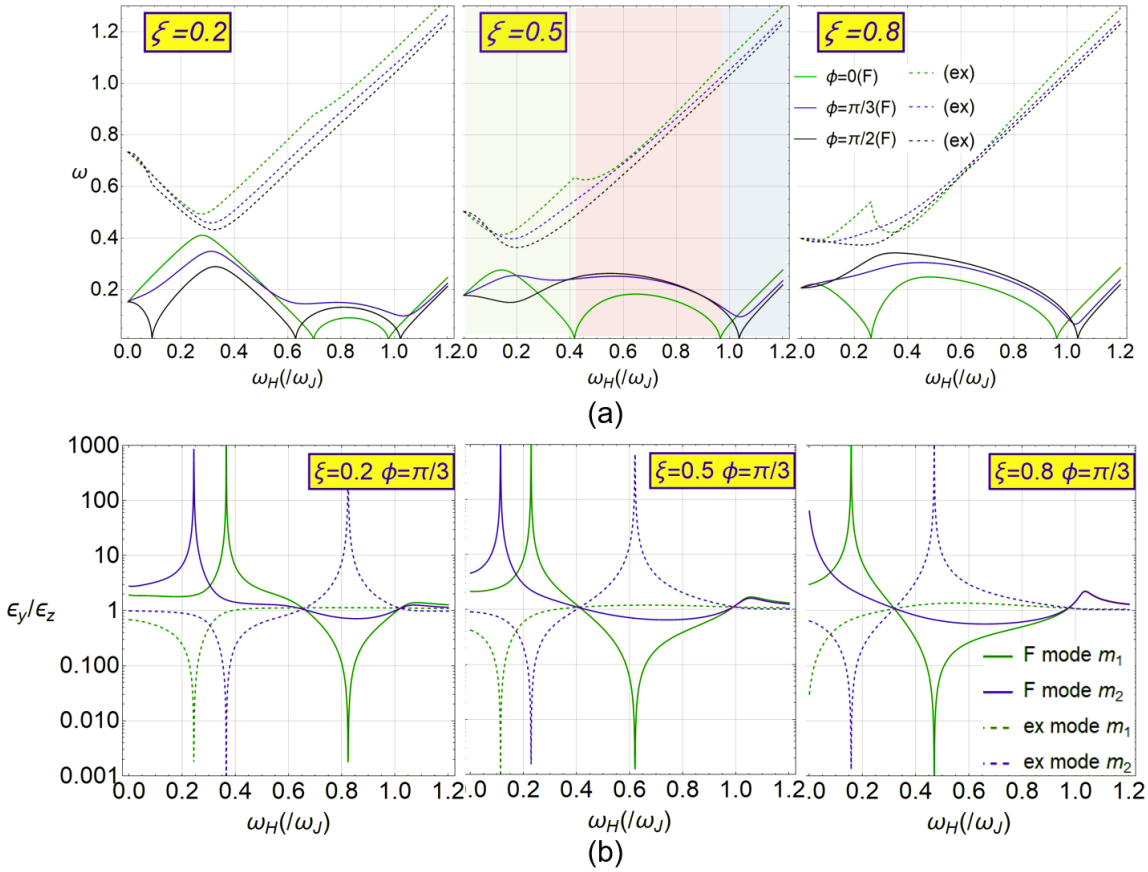

Figure 4.6: (a) Eigenfrequencies versus magnetic field along different in-plane directions for $\xi = 0.2$, 0.5, and 0.8. The collinear, SF, and spin-flip phases are shaded in different colors for the case of $\xi = 0.5$ and $\phi = 0$. (b) Polarization of each sublattice magnetic moment expressed as the ratio of the principal axes of elliptical trajectory in the local frame for $\phi = \pi/3$ at corresponding values of ξ. The diverging (vanishing) locations indicate linear polarization along the local in-plane Y (out-of-plane Z) direction. The first two divergences correspond to the two chirality flips depicted in Fig. 4.4. The third one takes place inside the SF phase.

Chapter 5

Van der Waals Antiferromagnets

5.1 Introduction

Van der Waals (vdW) antiferromagnets represent a fascinating class of materials within the broader context of two-dimensional (2D) layered systems. These materials are distinguished by their weak interlayer van der Waals forces, which facilitate easy exfoliation into atomically thin layers, like the widely recognized graphene. The antiferromagnetic nature of these materials adds an extra layer of intrigue, as they exhibit magnetic ordering without a net magnetization.

The exploration of vdW AF has accelerated in recent years, fueled by the discovery of new materials and the advancement of experimental techniques. These materials provide a unique platform to investigate fundamental physics, such as the interplay between magnetism, electronic structure, and topology. Furthermore, their 2D nature creates opportunities for integrating magnetism into heterostructures with other 2D materials, leading to innovative device concepts and functionalities.

5.2 $MnBi_2Te_4(Bi_2Te_3)_n$ Family

$MnBi_2Te_4(Bi_2Te_3)_n$ (with $n = 0, 1, 2$) serves as exemplary instances of vdW AF, being identified as a vdW magnetic topological insulator (MTI) with A-type antiferromagnetic ordering below their respective transition temperatures. The crystal structure of $MnBi_2Te_4(Bi_2Te_3)_n$ features an A-B-C stacking along the c-axis, which can be visualized as the insertion of non-magnetic quintuple Bi_2Te_3 layers into magnetic $MnBi_2Te_4$ layers demonstrated in Fig. 5.1. These layers are loosely bound by van der Waals exchange forces. As the number of quintuple layers increases, the van der Waals exchange interaction weakens, subsequently decreasing the magnetic field strength required to drive the resonance. The MBT family provides a unique platform for structural tuning of the interlayer exchange interaction by incorporating quintuple layers (QLs) to separate the ferromagnetic single layers (SLs). The electronic, magnetic, and thermodynamic properties of the MBT family have been extensively explored using techniques such as angle-resolved photoemission spectroscopy (ARPES), transport and magnetometry, magnetic force microscopy, and high-frequency electron spin resonance measurements. However, a comprehensive investigation through low-frequency magnetic resonance spectroscopy remains unreported. Previous high-frequency, high-field electron spin resonance (ESR) experiments demonstrated antiferromagnetic (AFM) spin excitations in $MnBi_2Te_4$ at fields up to saturation (approximately 6T), whereas only ferromagnetic (FM) excitations were observed in $MnBi_4Te_7$. The resonant field conditions in these sub-terahertz experiments, exceeding the spin-flip threshold.

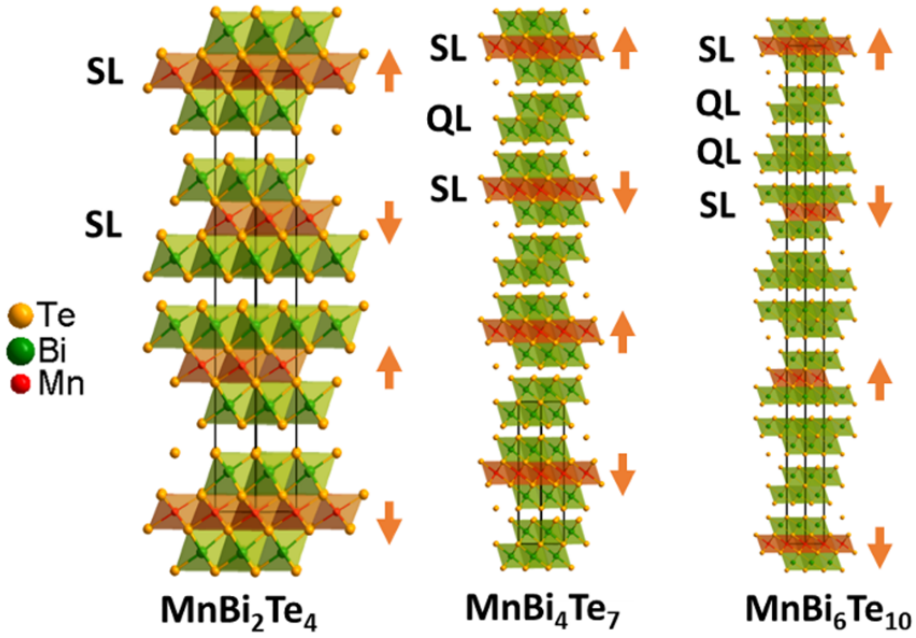

Figure 5.1: Crystal structures of $MnBi_2Te_4$, $MnBi_4Te_7$, and $MnBi_6Te_10$ with the growth direction or easy-axis aligned along the [0001] direction (c-axis). The magnetic layer containing Mn atoms is highlighted in orange, and the net magnetization of each Mn layer is indicated by an adjacent arrow. The non-magnetic quintuple Bi_2Te_3 layers and magnetic septuple $MnBi_2Te_4$ layers are labeled as QL and SL, respectively.

5.3 Field Rotations at Low Frequency

Our low-frequency spectroscopy measurements were conducted on single crystals of $MnBi_4Te_7$ and $MnBi_6Te_{10}$ at a temperature of $T = 7$ K, which is below the respective Néel temperatures of these compounds (reported to be 13 K and 11 K, respectively [72, 64]). The magnetic field was systematically applied at various angles within each of the three planes defined by the principal crystallographic axes, aiming to probe the anisotropic magnetic properties of these materials. Specific frequencies of 7 GHz for $MnBi_4Te_7$ and 8

GHz for $MnBi_6Te_{10}$ were employed to observe the resonant behavior associated with their antiferromagnetic ordering.

The geometry and orientation of the sample relative to the applied magnetic field are pivotal in interpreting the spectroscopic data. As depicted in Figure 5.2, the sample is positioned such that the a-b plane aligns with the y-z plane of the coordinate system, with the x-axis perpendicular to the sample plane. This configuration facilitates a systematic investigation of the impact of the magnetic field's orientation on the spin dynamics by varying the field direction within the defined planes.

Figure 5.3 presents the results obtained from the low-frequency spectroscopy measurements, both experimentally and theoretically, for $MnBi_4Te_7$. Rotations within the x-y and x-z planes correspond to out-of-plane (OOP) rotations with respect to the planar samples, while a rotation within the y-z plane corresponds to an in-plane (IP) rotation. These measurements were performed at $T = 7$ K, with the magnetic field swept from 0 to 1.2 T at various angles. A representative resonance curve, obtained for the field applied along the $+y$-axis, is shown in the inset of Figure 5.3(b) for reference.

The OOP field rotation on $MnBi_4Te_7$ in Figure 5.3(a) demonstrates a significant modulation of the resonance signal with respect to the applied field angle, showing a change of approximately 0.8 T in the resonance field position. An intense resonance occurs at a maximum field value of $H = 0.93$ T when the field is applied along the hard-axis (IP direction), and a minimum around $H = 0.17$ T when aligned with the easy magnetic x-axis (OOP direction).

This modulation of the resonance signal highlights the axial nature of the system,

consistent with the A-type easy-axis AF classification of this compound. When the magnetic field is aligned with the easy axis, the system enters a collinear phase. In this phase, as discussed in Chapter 3, the Néel vector contributes to spin pumping, requiring only a low magnetic field to achieve resonance. Conversely, when the magnetic field is applied along the y-direction, the system transitions to a non-collinear phase, detailed in Chapter 2. Here, the net magnetization, induced by canted magnetic moments, precesses in a more circular manner, enhancing spin pumping and requiring a higher external field to reach resonance.

5.4 Theoretical Analysis

The theoretical framework underpinning the results in Fig. 5.3 is based on the LLG equation, adapted for vdW AFs:

$$\begin{aligned}\dot{\boldsymbol{m}}_1 =& \omega_J \boldsymbol{m}_1 \times \boldsymbol{m}_2 - \omega_A \boldsymbol{m}_1 \times (\boldsymbol{m}_1 \cdot \hat{x})\hat{x} + \omega_K \boldsymbol{m}_1 \times (\boldsymbol{m}_1 \cdot \hat{y})\hat{y} \\ & - \omega_H \boldsymbol{m}_1 \times \hat{H} + \alpha \boldsymbol{m}_1 \times \dot{\boldsymbol{m}}_1, \end{aligned} \tag{5.1a}$$

$$\begin{aligned}\dot{\boldsymbol{m}}_2 =& \omega_J \boldsymbol{m}_2 \times \boldsymbol{m}_1 - \omega_A \boldsymbol{m}_2 \times (\boldsymbol{m}_2 \cdot \hat{x})\hat{x} + \omega_K \boldsymbol{m}_2 \times (\boldsymbol{m}_2 \cdot \hat{y})\hat{y} \\ & - \omega_H \boldsymbol{m}_2 \times \hat{H} + \alpha \boldsymbol{m}_2 \times \dot{\boldsymbol{m}}_2, \end{aligned} \tag{5.1b}$$

where $\hat{H}$ is the unit vector of the magnetic field $\boldsymbol{H}$, α represents the Gilbert damping constant, $\omega_J = J/\hbar$ denotes the exchange energy, which can be deduced from the Néel temperature or through first-principles calculations, both methods providing consistent outcomes. $\omega_A = A/\hbar$ and $\omega_K = K/\hbar$ represent the out-of-plane easy-axis and in-plane hard-axis anisotropy constants, respectively. Notably, in van der Waals materials, the exchange energy can be comparable to or even much smaller than the easy-axis anisotropy.

Therefore, by aligning characteristic values from experimental results, we can approximate the anisotropy parameters for $MnBi_4Te_7$ at $T = 7$ K as $\omega_A = 3.5\omega_J$ and $\omega_K = 1.6\omega_J$.

For magnetic field scanning in the x-y and x-z planes, the strong easy-axis anisotropy aligns with the magnetic field within a common plane, simplifying the problem to two dimensions. The inductions and results for these cases have been extensively discussed in Chapter 3, with the primary consideration being the variations in parameter values. However, the scenario differs significantly when scanning within the y-z plane. In this special case, the field-rotated plane is perpendicular to the easy axis, necessitating the treatment of a three-dimensional problem to adequately address the canting behavior of the magnetic moments.

The experimental reference frame is projected into the ground state local frame, which is determined by the magnetic field and the easy axis as illustrated in Fig. 5.4. For $\mathbf{m}_1$, the transformations are:

$$\hat{x} = \hat{x}_1 \cos\theta - \hat{y}_1 \sin\theta,$$

$$\hat{y} = \hat{x}_1 \sin\theta + \hat{y}_1 \cos\theta,$$

$$\hat{z} = \hat{z}_1.$$

For $\mathbf{m}_2$, the transformations are:

$$\hat{x} = -\hat{x}_2 \cos\theta - \hat{y}_2 \sin\theta,$$

$$\hat{y} = \hat{x}_2 \sin\theta - \hat{y}_2 \cos\theta,$$

$$\hat{z} = \hat{z}_2.$$

In this new geometry, the exchange energy and easy-axis retain similar forms, but

the anisotropy and Zeeman energy need to be reformulated for $\mathbf{m}_1$ and $\mathbf{m}_2$ as follows:

$$\begin{aligned}
\text{Hard axis anisotropy:}\quad & \omega_K \left(x_1 \sin\theta - y_1 \cos\theta\right) \cos^2\phi + \omega_K \left(x_2 \sin\theta + y_2 \cos\theta\right) \cos^2\phi, \\
\text{Zeeman energy:}\quad & -\omega_H \left(x_1 \sin\theta + y_1 \cos\theta\right) \cos\left(\phi - \phi_B\right) + \omega_H z_1 \sin\left(\phi - \phi_B\right) \\
& -\omega_H \left(x_2 \sin\theta - y_2 \cos\theta\right) \cos\left(\phi - \phi_B\right) + \omega_H z_2 \sin\left(\phi - \phi_B\right).
\end{aligned}$$

Where ϕ is the angle of the canting plane with respect to the y-axis. If there is no hard-axis anisotropy or the system holds rotational symmetry, then $\phi = \phi_B$. From this configuration, the 4×4 dynamical susceptibility tensor driven by the y-directional resonance field can be derived for the context of in-plane scanning.

$$\text{Column 1:}\quad \begin{bmatrix} \left(i\alpha\omega + \omega_A \cos(2\theta) + \omega_J \cos(2\theta) + \omega_K \cos(2\theta)\cos^2(\phi) + \omega_H \sin(\theta)\cos(\phi - \phi_B)\right) \\ -\omega_J \cos(2\theta) \\ i\omega \\ 0 \end{bmatrix} \tag{5.2}$$

$$\text{Column 2:}\quad \begin{bmatrix} -\omega_J \cos(2\theta) \\ \left(i\alpha\omega + \omega_A \cos(2\theta) + \omega_J \cos(2\theta) + \omega_K \cos(2\theta)\cos^2(\phi) + \omega_H \sin(\theta)\cos(\phi - \phi_B)\right) \\ 0 \\ i\omega \end{bmatrix} \tag{5.3}$$

$$\text{Column 3:} \quad \begin{bmatrix} -\omega_J \cos(2\theta) \\ 0 \\ \left(\begin{array}{c} i\alpha\omega + \omega_A \cos^2(\theta) + \omega_J \cos(2\theta) - \omega_K \sin^2(\theta)\cos^2(\phi) \\ + \omega_H \sin(\theta)\cos(\phi - \phi_B) + \omega_K \sin^2(\phi) \end{array} \right) \\ \omega_J \end{bmatrix} \tag{5.4}$$

$$\text{Column 4:} \quad \begin{bmatrix} 0 \\ i\omega \\ \omega_J \\ \left(\begin{array}{c} i\alpha\omega + \omega_A \cos^2(\theta) + \omega_J \cos(2\theta) - \omega_K \sin^2(\theta)\cos^2(\phi) \\ + \omega_H \sin(\theta)\cos(\phi - \phi_B) + \omega_K \sin^2(\phi) \end{array} \right) \end{bmatrix} \tag{5.5}$$

Next, the spin current signal generated by an x-polarized (laboratory frame) microwave magnetic field will be obtained in Fig. 5.3(f), where a crescent-shape signal can be found along the in-plane z-axis, consistent with the experimental observation.

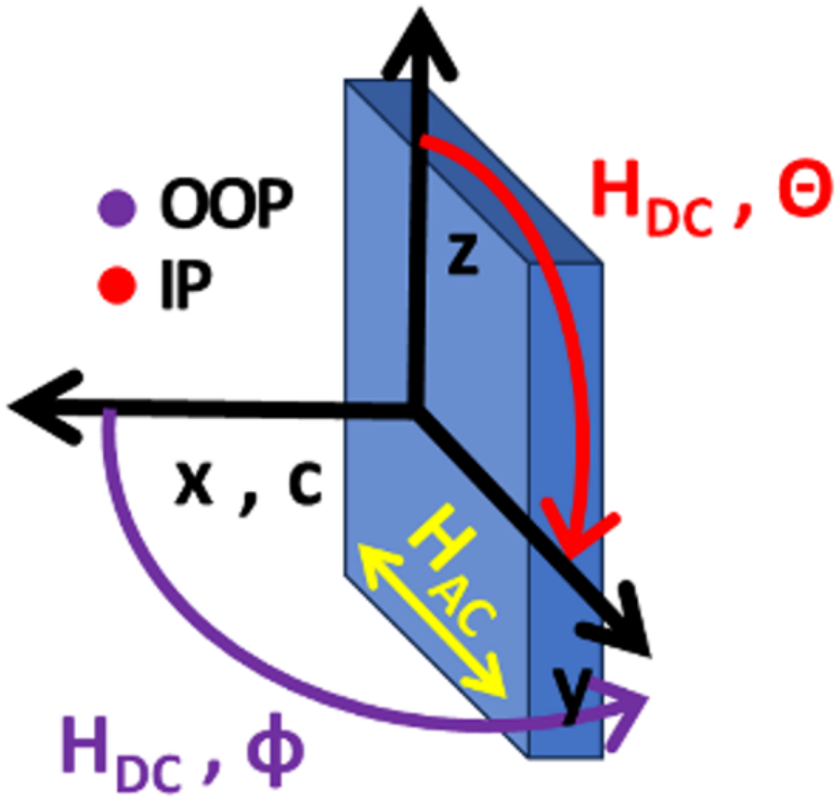

Figure 5.2: Sketch of a coplanar waveguide (CPW) with a ground-source-ground configuration utilized in the measurement setup. The sample is positioned on top of the highly sensitive constricted central region of the CPW. The chosen coordinate system with respect to the CPW is also depicted. The a-b plane of the sample aligns with the y-z plane of the chosen coordinate system, with the x-axis perpendicular to the sample plane. The y-axis corresponds to the direction parallel to the microwave AC field. The polar angles θ and ϕ account for the direction of the applied DC magnetic field H.

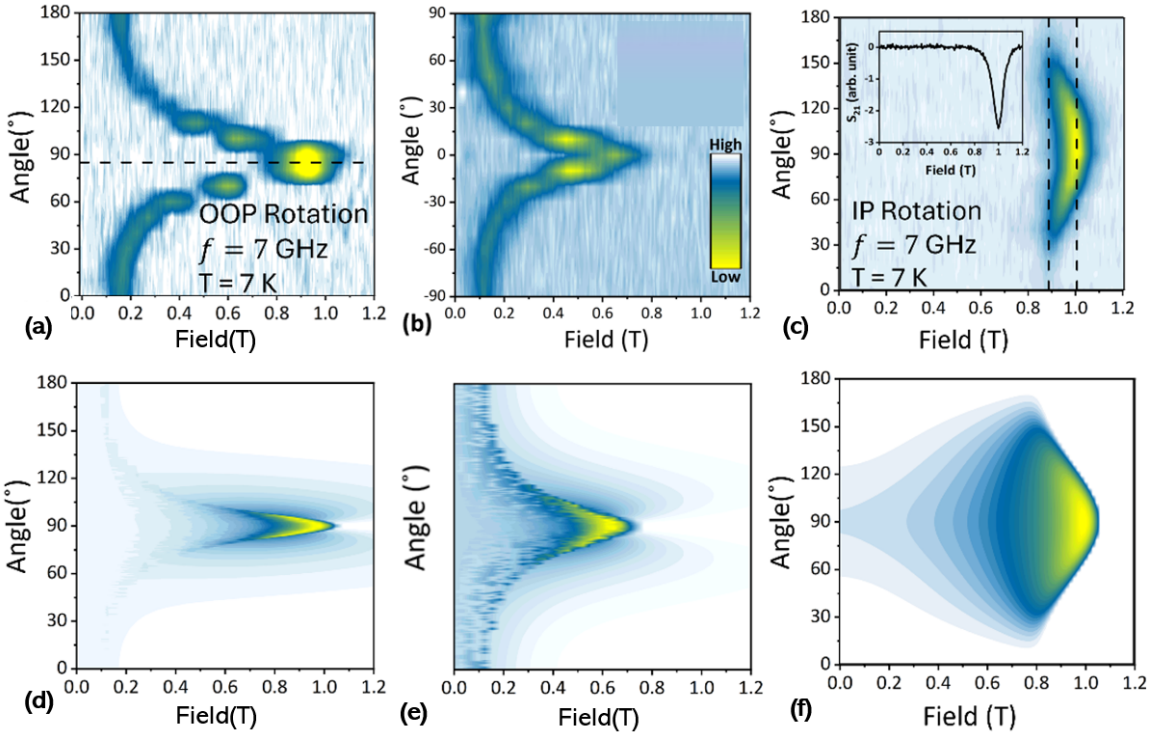

Figure 5.3: Results for in-plane (IP) field rotations (a-b) and out-of-plane (OOP) field rotations (c) measured on $MnBi_4Te_7$ at $T = 7$ K and frequency $f = 7$ GHz. Corresponding theoretical results are illustrated in (d-f). A representative sample resonance signal is shown in the inset of (b).

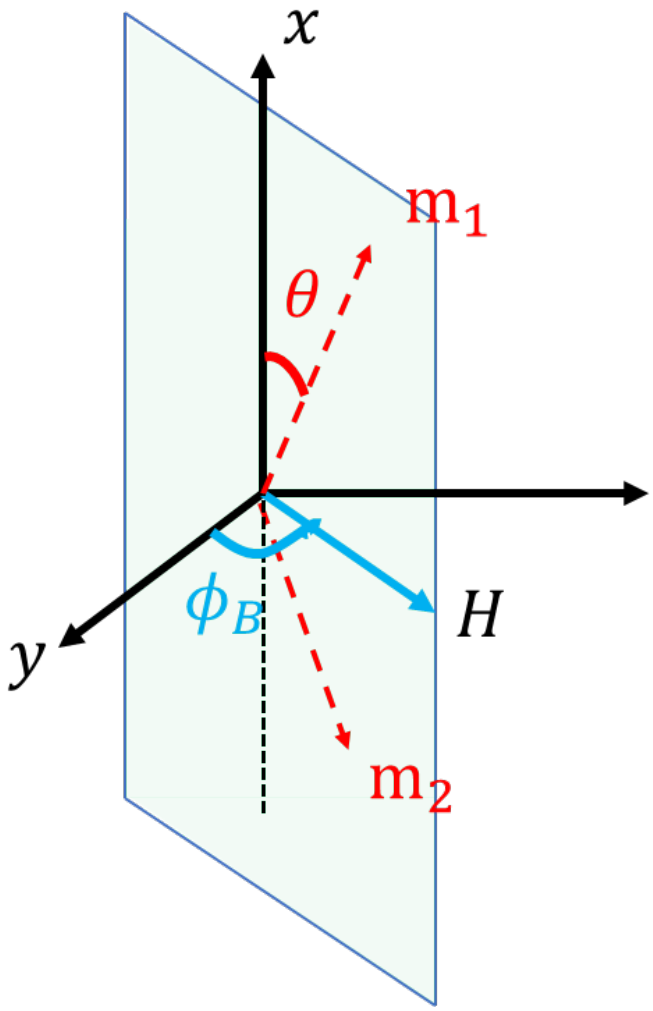

Figure 5.4: Illustration of the ground state local frame determined by the magnetic field and the easy axis. Here, ϕ_B represents the angle of the external magnetic field with respect to the y-axis, and θ is the cant angle of the magnetic moments with respect to the easy axis.

Chapter 6

Conclusions

6.1 Summary and Conclusion

We are now in a good position to conclude the long journey of antiferromagnetic spintronics. We have explored the intricate dynamics of spin pumping and spin transfer torque in antiferromagnetic and ferrimagnetic materials, shedding light on the fundamental mechanisms that govern these phenomena. Our investigation into van der Waals antiferromagnets has unveiled their unique properties and potential for integration into spintronic devices.

Through a combination of theoretical analysis and experimental observations, it has demonstrated how the interplay between magnetic anisotropies, exchange interactions, and external magnetic fields influences the behavior of magnetic moments in these materials. The findings reveal the critical role of the Dzyaloshinskii-Moriya interaction in enhancing spin pumping efficiency and the significant impact of magnetic field orientation on the detection of antiferromagnetic resonance signals.

Moreover, our study extends to the realm of ferrimagnets, where we have identified the advantages of utilizing these materials in spintronic applications due to their non-vanishing magnetization. By tuning the ratio of sublattice spins, we have established a generic picture that bridges the gap between ferromagnetic and antiferromagnetic limits, offering insights into the spin dynamics across a wide range of ferrimagnetic systems.

In summary, this research contributes to a deeper understanding of spin dynamics in antiferromagnetic and ferrimagnetic materials, paving the way for the development of high-speed, energy-efficient spintronic devices. The unique properties of van der Waals antiferromagnets open up new avenues for exploring topological phenomena and integrating magnetism into two-dimensional heterostructures. Further advancements in the field of spintronics are anticipated, with potential applications in information storage, quantum computing, and beyond.

6.2 Outlook

Future research directions in antiferromagnetic spintronics are rich with potential, building on the foundations laid by the investigations presented in this dissertation.

One intriguing aspect of antiferromagnetic spintronics is the propagation of spin currents across interfaces between ferromagnets and antiferromagnets. The atomic-scale interactions at these interfaces can give rise to unique properties that are not observed in bulk materials. For instance, the interplay between spin-transfer torque and exchange bias at the interface can lead to novel phenomena such as spin current-induced switching in antiferromagnets. Investigating these effects at the atomic level will provide insights

into the mechanisms governing spin current propagation and open up new possibilities for spintronic device engineering.

The emergence of van der Waals antiferromagnets has opened up new opportunities for integrating magnetism into two-dimensional heterostructures. These materials offer a unique platform for studying the interplay between magnetism, electronic structure, and topology in atomically thin layers. Future research will focus on understanding the fundamental properties of van der Waals antiferromagnets and exploring their potential for applications in spintronic devices, sensors, and quantum computing.

While the single-electron approximation has been a useful starting point, incorporating many-body effects and non-adiabatic dynamics into theoretical models is essential for a more comprehensive understanding of spintronics. These effects are particularly relevant in materials with strong electron-electron interactions and in systems where the spin dynamics occur on timescales comparable to the electronic relaxation times. Developing models that account for these complexities will enable more accurate predictions of spintronic device behavior and guide the design of new materials and structures.

The field of antiferromagnetic spintronics is poised for significant advancements, with a wide range of promising research directions. Our study guides through a variety of ways to realize the novel functioning of antiferromagnetic materials in different situations. We can expect to uncover new physical phenomena and develop innovative technologies that harness the unique properties of antiferromagnetic materials.

Bibliography

[1] Vincent Baltz, Aurelien Manchon, M Tsoi, Takahiro Moriyama, T Ono, and Y Tserkovnyak. Antiferromagnetic spintronics. *Reviews of Modern Physics*, 90(1):015005, 2018.

[2] Anjan Barman, T Kimura, Y Otani, Y Fukuma, K Akahane, and S Meguro. Benchtop time-resolved magneto-optical kerr magnetometer. *Review of Scientific Instruments*, 79(12), 2008.

[3] J. Becker, A. Tsukamoto, A. Kirilyuk, J. C. Maan, Th. Rasing, P. C. M. Christianen, and A. V. Kimel. Ultrafast Magnetism of a Ferrimagnet across the Spin-Flop Transition in High Magnetic Fields. *Physical Review Letters*, 118(11):117203, 2017.

[4] Luc Berger. Emission of spin waves by a magnetic multilayer traversed by a current. *Physical Review B*, 54(13):9353, 1996.

[5] Isabella Boventer, Haakon T Simensen, A Anane, Mathias Kläui, Arne Brataas, and Romain Lebrun. Room-temperature antiferromagnetic resonance and inverse spin-Hall voltage in canted antiferromagnets. *Physical review letters*, 126(18):187201, 2021.

[6] Arne Brataas, Yaroslav Tserkovnyak, Gerrit EW Bauer, and Bertrand I Halperin. Spin battery operated by ferromagnetic resonance. *Physical Review B*, 66(6):060404, 2002.

[7] Guido Burkard, Hans-Andreas Engel, and Daniel Loss. Spintronics and quantum dots for quantum computing and quantum communication. *Fortschritte der Physik: Progress of Physics*, 48(9-11):965–986, 2000.

[8] Cui-Zu Chang, Jinsong Zhang, Xiao Feng, Jie Shen, Zuocheng Zhang, Minghua Guo, Kang Li, Yunbo Ou, Pang Wei, Li-Li Wang, et al. Experimental observation of the quantum anomalous hall effect in a magnetic topological insulator. *Science*, 340(6129):167–170, 2013.

[9] Claude Chappert, Albert Fert, and Frédéric Nguyen Van Dau. The emergence of spin electronics in data storage. *Nature materials*, 6(11):813–823, 2007.

[10] Hetian Chen and Di Yi. Spin–charge conversion in transition metal oxides. *APL Materials*, 9(6), 2021.

[11] Ran Cheng, Matthew W Daniels, Jian-Gang Zhu, and Di Xiao. Ultrafast switching of antiferromagnets via spin-transfer torque. *Physical Review B*, 91(6):064423, 2015.

[12] Ran Cheng, Matthew W. Daniels, Jian-Gang Zhu, and Di Xiao. Ultrafast switching of antiferromagnets via spin-transfer torque. *Phys. Rev. B*, 91:064423, Feb 2015.

[13] Ran Cheng, Di Xiao, and Arne Brataas. Terahertz antiferromagnetic spin hall nano-oscillator. *Physical review letters*, 116(20):207603, 2016.

[14] Ran Cheng, Jiang Xiao, Qian Niu, and Arne Brataas. Spin pumping and spin-transfer torques in antiferromagnets. *Physical review letters*, 113(5):057601, 2014.

[15] Tomasz Dietl and Hideo Ohno. Dilute ferromagnetic semiconductors: Physics and spintronic structures. *Reviews of Modern Physics*, 86(1):187, 2014.

[16] Anas El Hamdi, Jean-Yves Chauleau, Margherita Boselli, Clémentine Thibault, Cosimo Gorini, Alexander Smogunov, Cyrille Barreteau, Stefano Gariglio, Jean-Marc Triscone, and Michel Viret. Observation of the orbital inverse rashba–edelstein effect. *Nature Physics*, 19(12):1855–1860, 2023.

[17] Joseph Finley and Luqiao Liu. Spintronics with compensated ferrimagnets. *Applied Physics Letters*, 116(11):110501, 2020.

[18] Regina Galceran, Bo Tian, Junzhu Li, Frédéric Bonell, Matthieu Jamet, Céline Vergnaud, Alain Marty, Jose H García, Juan F Sierra, Marius V Costache, et al. Control of spin–charge conversion in van der waals heterostructures. *APL Materials*, 9(10), 2021.

[19] EV Gomonay and VM Loktev. Spintronics of antiferromagnetic systems. *Low Temperature Physics*, 40(1):17–35, 2014.

[20] Cheng Gong and Xiang Zhang. Two-dimensional magnetic crystals and emergent heterostructure devices. *Science*, 363(6428):eaav4450, 2019.

[21] Paul M. Haney and A. H. MacDonald. Current-induced torques due to compensated antiferromagnets. *Phys. Rev. Lett.*, 100:196801, May 2008.

[22] Axel Hoffmann and Sam D Bader. Opportunities at the frontiers of spintronics. *Physical Review Applied*, 4(4):047001, 2015.

[23] Chaowei Hu, Kyle N Gordon, Pengfei Liu, Jinyu Liu, Xiaoqing Zhou, Peipei Hao, Dushyant Narayan, Eve Emmanouilidou, Hongyi Sun, Yuntian Liu, et al. A van der waals antiferromagnetic topological insulator with weak interlayer magnetic coupling. *Nature communications*, 11(1):97, 2020.

[24] Bevin Huang, Genevieve Clark, Efrén Navarro-Moratalla, Dahlia R Klein, Ran Cheng, Kyle L Seyler, Ding Zhong, Emma Schmidgall, Michael A McGuire, David H Cobden, et al. Layer-dependent ferromagnetism in a van der waals crystal down to the monolayer limit. *Nature*, 546(7657):270–273, 2017.

[25] HuJun Jiao and Gerrit EW Bauer. Spin backflow and ac voltage generation by spin pumping and the inverse spin Hall effect. *Physical review letters*, 110(21):217602, 2013.

[26] Øyvind Johansen and Arne Brataas. Spin pumping and inverse spin Hall voltages from dynamical antiferromagnets. *Physical Review B*, 95(22):220408, 2017.

[27] T Jungwirth, J Sinova, Aurelien Manchon, X Marti, J Wunderlich, and C Felser. The multiple directions of antiferromagnetic spintronics. *Nature Physics*, 14(3):200–203, 2018.

[28] Tomas Jungwirth, X Marti, P Wadley, and J Wunderlich. Antiferromagnetic spintronics. *Nature nanotechnology*, 11(3):231–241, 2016.

[29] Tomas Jungwirth, Jörg Wunderlich, and Kamil Olejník. Spin hall effect devices. *Nature materials*, 11(5):382–390, 2012.

[30] Sangita S Kalarickal, Pavol Krivosik, Mingzhong Wu, Carl E Patton, Michael L Schneider, Pavel Kabos, Thomas J Silva, and John P Nibarger. Ferromagnetic resonance linewidth in metallic thin films: Comparison of measurement methods. *Journal of Applied Physics*, 99(9), 2006.

[31] F Keffer and Ch Kittel. Theory of antiferromagnetic resonance. *Physical Review*, 85(2):329, 1952.

[32] Roman Khymyn, Ivan Lisenkov, Vasyl Tiberkevich, Boris A Ivanov, and Andrei Slavin. Antiferromagnetic THz-frequency Josephson-like oscillator driven by spin current. *Scientific reports*, 7(1):1–10, 2017.

[33] Changsoo Kim, Soogil Lee, Hyun-Gyu Kim, Ji-Ho Park, Kyung-Woong Moon, Jae Yeol Park, Jong Min Yuk, Kyung-Jin Lee, Byong-Guk Park, Se Kwon Kim, et al. Distinct handedness of spin wave across the compensation temperatures of ferrimagnets. *Nature Materials*, 19(9):980–985, 2020.

[34] Se Kwon Kim, Geoffrey SD Beach, Kyung-Jin Lee, Teruo Ono, Theo Rasing, and Hyunsoo Yang. Ferrimagnetic spintronics. *Nature materials*, 21(1):24–34, 2022.

[35] Seok-Jong Kim, Dong-Kyu Lee, Se-Hyeok Oh, Hyun Cheol Koo, and Kyung-Jin Lee. Theory of spin-torque ferrimagnetic resonance. *Physical Review B*, 104(2):024405, 2021.

[36] Charles Kittel. On the gyromagnetic ratio and spectroscopic splitting factor of ferromagnetic substances. *Phys. Rev.*, 76:743–748, Sep 1949.

[37] Jiaheng Li, Yang Li, Shiqiao Du, Zun Wang, Bing-Lin Gu, Shou-Cheng Zhang, Ke He, Wenhui Duan, and Yong Xu. Intrinsic magnetic topological insulators in van der waals layered mnbi2te4-family materials. *Science Advances*, 5(6):eaaw5685, 2019.

[38] Junxue Li, C Blake Wilson, Ran Cheng, Mark Lohmann, Marzieh Kavand, Wei Yuan, Mohammed Aldosary, Nikolay Agladze, Peng Wei, Mark S Sherwin, et al. Spin current from sub-terahertz-generated antiferromagnetic magnons. *Nature*, 578(7793):70–74, 2020.

[39] EM Lifshitz. Pitaevskii: Statistical physics, part2. *Course of Theoretical Physics, Vol. 9*, 369, 1989.

[40] Jun Liu, Gyung-Min Choi, and David G Cahill. Measurement of the anisotropic thermal conductivity of molybdenum disulfide by the time-resolved magneto-optic kerr effect. *Journal of Applied Physics*, 116(23), 2014.

[41] AH MacDonald and M Tsoi. Antiferromagnetic metal spintronics. *Philosophical Transactions of the Royal Society A: Mathematical, Physical and Engineering Sciences*, 369(1948):3098–3114, 2011.

[42] FLA Machado, PRT Ribeiro, J Holanda, RL Rodríguez-Suárez, A Azevedo, and SM Rezende. Spin-flop transition in the easy-plane antiferromagnet nickel oxide. *Physical Review B*, 95(10):104418, 2017.

[43] Aurelien Manchon, Jakub Železnỳ, Ioan M Miron, Tomáš Jungwirth, Jairo Sinova, André Thiaville, Kevin Garello, and Pietro Gambardella. Current-induced spin-orbit torques in ferromagnetic and antiferromagnetic systems. *Reviews of Modern Physics*, 91(3):035004, 2019.

[44] Tôru Moriya. Theory of Magnetism of NiF2. *Physical Review*, 117(3):635–647, 1960.

[45] Takahiro Moriyama, Kensuke Hayashi, Keisuke Yamada, Mutsuhiro Shima, Yutaka Ohya, and Teruo Ono. Intrinsic and extrinsic antiferromagnetic damping in NiO. *Physical Review Materials*, 3(5):051402, 2019.

[46] T Nagamiya, K Yosida, and R Kubo. Antiferromagnetism. *Advances in Physics*, 4(13):1–112, 1955.

[47] Lars Onsager. Reciprocal relations in irreversible processes. i. *Physical review*, 37(4):405, 1931.

[48] Lars Onsager. Reciprocal relations in irreversible processes. ii. *Physical review*, 38(12):2265, 1931.

[49] Mikhail M Otrokov, Ilya I Klimovskikh, Hendrik Bentmann, D Estyunin, Alexander Zeugner, Ziya S Aliev, S Gaß, AUB Wolter, AV Koroleva, Alexander M Shikin, et al. Prediction and observation of an antiferromagnetic topological insulator. *Nature*, 576(7787):416–422, 2019.

[50] Jorge Puebla, Junyeon Kim, Kouta Kondou, and Yoshichika Otani. Spintronic devices for energy-efficient data storage and energy harvesting. *Communications Materials*, 1(1):24, 2020.

[51] Sergio M Rezende, Antonio Azevedo, and Roberto L Rodríguez-Suárez. Introduction to antiferromagnetic magnons. *Journal of Applied Physics*, 126(15):151101, 2019.

[52] J-C Rojas-Sánchez, M Cubukcu, A Jain, C Vergnaud, C Portemont, C Ducruet, A Barski, A Marty, L Vila, J-P Attané, et al. Spin pumping and inverse spin hall effect in germanium. *Physical Review B*, 88(6):064403, 2013.

[53] A Safin, V Puliafito, M Carpentieri, G Finocchio, S Nikitov, P Stremoukhov, A Kirilyuk, V Tyberkevych, and A Slavin. Electrically tunable detector of THz-frequency signals based on an antiferromagnet. *Applied Physics Letters*, 117(22):222411, 2020.

[54] Ansar Safin, Sergey Nikitov, Andrei Kirilyuk, Vasyl Tyberkevych, and Andrei Slavin. Theory of antiferromagnet-based detector of terahertz frequency signals. *Magnetochemistry*, 8(2):26, 2022.

[55] Hamed Ben Mohamed Saidaoui, Aurelien Manchon, and Xavier Waintal. Spin transfer torque in antiferromagnetic spin valves: From clean to disordered regimes. *Physical Review B*, 89(17):174430, 2014.

[56] G. G. Scott. Review of gyromagnetic ratio experiments. *Rev. Mod. Phys.*, 34:102–109, Jan 1962.

[57] Ankit Shukla and Shaloo Rakheja. Spin-torque-driven terahertz auto-oscillations in noncollinear coplanar antiferromagnets. *Physical Review Applied*, 17(3):034037, 2022.

[58] AJ Sievers III and M Tinkham. Far infrared antiferromagnetic resonance in MnO and NiO. *Physical Review*, 129(4):1566, 1963.

[59] Jairo Sinova, Sergio O Valenzuela, Jörg Wunderlich, CH Back, and T Jungwirth. Spin hall effects. *Reviews of modern physics*, 87(4):1213, 2015.

[60] John C Slonczewski. Current-driven excitation of magnetic multilayers. *Journal of Magnetism and Magnetic Materials*, 159(1-2):L1–L7, 1996.

[61] OR Sulymenko, OV Prokopenko, VS Tiberkevich, AN Slavin, BA Ivanov, and RS Khymyn. Terahertz-frequency spin hall auto-oscillator based on a canted antiferromagnet. *Physical Review Applied*, 8(6):064007, 2017.

[62] Yoshinori Tokura, Kenji Yasuda, and Atsushi Tsukazaki. Magnetic topological insulators. *Nature Reviews Physics*, 1(2):126–143, 2019.

[63] Priyanka Vaidya, Sophie A Morley, Johan van Tol, Yan Liu, Ran Cheng, Arne Brataas, David Lederman, and Enrique Del Barco. Subterahertz spin pumping from an insulating antiferromagnet. *Science*, 368(6487):160–165, 2020.

[64] Raphael C Vidal, Alexander Zeugner, Jorge I Facio, Rajyavardhan Ray, M Hossein Haghighi, Anja UB Wolter, Laura T Corredor Bohorquez, Federico Caglieris, Simon Moser, Tim Figgemeier, et al. Topological electronic structure and intrinsic magnetization in MnBi4Te7: a Bi2Te3 derivative with a periodic Mn sublattice. *Physical Review X*, 9(4):041065, 2019.

[65] Giovanni Vignale and IV Tokatly. Theory of the nonlinear rashba-edelstein effect: The clean electron gas limit. *Physical Review B*, 93(3):035310, 2016.

[66] Hailong Wang, Yuxuan Xiao, Mingda Guo, Eric Lee-Wong, Gerald Q Yan, Ran Cheng, and Chunhui Rita Du. Spin Pumping of an Easy-Plane Antiferromagnet Enhanced by Dzyaloshinskii–Moriya Interaction. *Physical Review Letters*, 127(11):117202, 2021.

[67] Yuyan Wang, Martin M Decker, Thomas NG Meier, Xianzhe Chen, Cheng Song, Tobias Grünbaum, Weisheng Zhao, Junying Zhang, Lin Chen, and Christian H Back. Spin pumping during the antiferromagnetic–ferromagnetic phase transition of iron–rhodium. *Nature Communications*, 11(1):275, 2020.

[68] YY Wang, Cheng Song, JY Zhang, and Feng Pan. Spintronic materials and devices based on antiferromagnetic metals. *Progress in Natural Science: Materials International*, 27(2):208–216, 2017.

[69] Roald K. Wangsness. Sublattice Effects in Magnetic Resonance. *Physical Review*, 91(5):1085–1091, 1953.

[70] Samuel J Williamson and Simon Foner. Antiferromagnetic Resonance in Systems with Dzyaloshinsky-Moriya Coupling; Orientation Dependence in α-Fe2O3. *Physical Review*, 136(4A):A1102, 1964.

[71] SA Wolf, DD Awschalom, RA Buhrman, JM Daughton, von S von Molnár, ML Roukes, A Yu Chtchelkanova, and DM Treger. Spintronics: a spin-based electronics vision for the future. *science*, 294(5546):1488–1495, 2001.

[72] J-Q Yan, YH Liu, DS Parker, Y Wu, AA Aczel, M Matsuda, MA McGuire, and BC Sales. A-type antiferromagnetic order in mnbi 4 te 7 and mnbi 6 te 10 single crystals. *Physical Review Materials*, 4(5):054202, 2020.

[73] Fengyuan Yang and P Chris Hammel. Fmr-driven spin pumping in y3fe5o12-based structures. *Journal of Physics D: Applied Physics*, 51(25):253001, 2018.

[74] J Železnỳ, P Wadley, K Olejník, A Hoffmann, and H Ohno. Spin transport and spin torque in antiferromagnetic devices. *Nature Physics*, 14(3):220–228, 2018.

[75] Chi Zhang, Yong Pu, Sergei A Manuilov, Denis V Pelekhov, and P Chris Hammel. Spin-torque ferromagnetic resonance (st-fmr) spectroscopy of localized spin wave modes engineered by applied dipole-field localization. In *APS March Meeting Abstracts*, volume 2016, pages L6–008, 2016.

[76] C Zhou, YP Liu, Z Wang, SJ Ma, M Wu Jia, RQ Wu, L Zhou, W Zhang, MK Liu, YZ Wu, et al. Broadband terahertz generation via the interface inverse rashba-edelstein effect. *Physical review letters*, 121(8):086801, 2018.